WORLD OCEAN CIRCULATION

ALGORITHM THEORETICAL BASIS DOCUMENT FOR ERA STAR (THEME 1)

customer	ESA/ESRIN
ESA contract	ESA Contract No. 4000130730/20/I-NB
document reference	WOC-ESA-ODL-NR-009_T1_ERAstar_V2.0
Version/Rev	2.0
Date of issue	30/06/2022

World Ocean Circulation
Project Management Plan

Ref.: WOC-ESA-ODL-NR-
009_T1_ERAstar
Date: 30/06/2022
Issue: 2.0

Distribution List

	Name	**Organization**	**Nb. copies**
Sent to :	M.H. Rio	ESA/ESRIN	ESAstar
Internal copy :	Project Manager	OceanDatalab	1 (digital copy)

Document evolution sheet

Ed.	**Rev.**	**Date**	**Purpose evolution**	**Comments**
1	0	25/06/2021	Creation of document	
2	0	30/06/2022	Version 2	

	Name	**Company**	**Date**	**Signature**
Prepared by :	M. Portabella, A. Trindade, G. Grieco E. Makarova	ICM-CSIC ICM-CSIC/UPC ISMAR-CNR ICM-CSIC	30/06/2022	
Checked by :				
Approved by :				

World Ocean Circulation
Project Management Plan

Ref.: WOC-ESA-ODL-NR-
009_T1_ERAstar
Date: 30/06/2022
Issue: 2.0

Contents

List of Images

List of Tables

World Ocean Circulation
Project Management Plan

Ref.: WOC-ESA-ODL-NR-
009_T1_ERAstar
Date: 30/06/2022
Issue: 2.0

1 Introduction

1.1 Product summary

The ERA* stress-equivalent wind (U10S) and stress vector product is a correction of the ECMWF Fifth Reanalysis (ERA5) output by means of geo-located scatterometer-ERA5 differences over a few days temporal window. The version 2 products contain two different datasets: the nominal product over the period 2010-2020, which uses a temporal window of 15 days (except for 2010, in which a temporal window of 30 days is used); and an enhanced quality and resolution product for the years 2013, 2018 and 2020, which uses a temporal window of 3 days. Both products use, at any given time, all available scatterometer systems with global and continuous coverage. The enhanced product is only provided over those periods in which there is sufficient scatterometer sampling to allow the use of short temporal windows. The scatterometer-based corrections are computed from a combination of the following systems, i.e., the Advanced Scatterometers (ASCAT-A, -B, -C) onboard the EUMETSAT Metop satellite series, and the scatterometers onboard the ISRO Oceansat-2 (OSCAT) and SCATSat-1 (OSCAT2). ERA* can correct for local, persistent NWP model output errors associated with physical processes that are absent or misrepresented by the model, e.g., strong current effects (such as WBCS, highly stationary), wind effects associated with the ocean mesoscales (SST), coastal effects (land see breezes, katabatic winds), PBL parameterization errors, and large-scale circulation effects, e.g., at the ITCZ.

1.2 Scope & Objectives

This document holds the Algorithm Theoretical Baseline (ATBD) prepared by the WOC team, as part of the activities included in Theme 1 of the Proposal (SoW ref. EOP-SD-SOW-0092). The main objective of this document is to provide a detailed definition of the algorithm used to generate the second version of the following products:

- ERA* U10S & stress

1.3 Document structure

In addition to this introduction, this document includes the following chapter:

- Chapter 2 describes the development of the ERA* algorithm and the ERA* product verification.

World Ocean Circulation
Project Management Plan

Ref.: WOC-ESA-ODL-NR-
009_T1_ERAstar
Date: 30/06/2022
Issue: 2.0

1.4 Applicable & Reference documents

- [RD-1] ESA WOC2019: http://woc2019.esa.int/index.php

- [RD-2] Synthesis of the WOC2019 User Consultation Meeting recommendations http://woc2019.esa.int/files/WOC2019_summary_synthesis.pdf

1.5 Terminology

ASCAT	Advanced SCATterometer on board Metop satellite series
ATBD	Algorithm Theoretical Basis Document
BUFR	Binary Universal Form for the Representation of meteorological data
CMEMS	Copernicus Marine Environment Monitoring Service
ECMWF	European Centre for Medium-Range Weather Forecasts
ERA5	Fifth ECMWF Reanalysis
ESA	European Space Agency
FC	Forecast
GRIB	GRIdded Binary or General Regularly-distributed Information in Binary form
HSCAT-A	HY-2A scatterometer
HSCAT-B	HY-2B scatterometer
IFREMER	Institut Français de Recherche pour l'Exploitation de la Mer
ITCZ	InterTropical Convergence Zone
KNMI	Royal Netherlands Meteorological Institute
NOAA	National Oceanic and Atmospheric Administration
OSCAT	Oceansat-2 SCATterometer
OSCAT2	SCATSat-1 scatterometer
PUM	Product User Manual
QUID	Quality Information Document
RB	Requirement Baseline
SSH	Sea Surface Height
SSS	Sea Surface Salinity
SST	Sea Surface Temperature
SoW	Statement of Work
TN	Technical Note
U10S	Stress-equivalent wind
UCM	User Consultation Meeting

World Ocean Circulation
Project Management Plan

Ref.: WOC-ESA-ODL-NR-
009_T1_ERAstar
Date: 30/06/2022
Issue: 2.0

URD	User Requirement Document
WBS	Work Breakdown Structure
WOC	World Ocean Circulation

World Ocean Circulation
Project Management Plan

Ref.: WOC-ESA-ODL-NR-
009_T1_ERAstar
Date: 30/06/2022
Issue: 2.0

2 ERA star

High-resolution ocean modelling studies are essential to understand the processes that occur in the ocean and at the sea surface. Because much of the ocean's variability, especially in the top layers, is wind driven, it is crucial to choose an accurate wind forcing product, which is able to resolve the fine ocean scales. Scatterometers provide high resolution surface wind measurements, but only twice a day. In the absence of high spatial and temporal resolution global sea surface wind data observations, Numerical Weather Prediction (NWP) forcing products are widely used in ocean forecasting. Among the most commonly simulated atmospheric wind fields are those generated by the Integrated Forecast System (IFS) or Global Circulation Models (GCM), e.g., the European Centre for Medium-range Weather Forecasts (ECMWF) fifth reanalysis or ERA5 [Hersbach et al., 2020], or locally downscaled versions of it.

Although ubiquitous, prior to being used as ocean forcing (i.e., wind stress), the NWP output requires additional information on ocean currents, atmospheric stratification and mass density. Moreover, although frequently used for ocean simulations, several issues with global NWP output (like ERA5) have been reported, e.g., large-scale circulation errors [Belmonte-Rivas and Stoffelen, 2019], misplacement of fronts and depressions, poorly resolved small-scale dynamics, such as those associated with moist convection [King et al., 2017], or lack of cross-isobaric flow (i.e., NWP wind directions are biased with respect to the observed winds with opposite sign in the Southern and the Northern Hemispheres, particularly in stable stratification) [Hersbach, 2010], [Brown et al., 2005], [Sandu et al., 2013].

In contrast, ocean surface vector winds derived from scatterometers onboard Earth Observation (EO) satellites, although intrinsically limited by temporal and spatial sampling, exhibit considerable spatial detail and accuracy on the sea surface winds [Vogelzang et al., 2011], [Lin et al., 2015a]. In addition, while NWP wind outputs are relative to a fixed Earth grid, scatterometers measure the wind relative to the moving ocean surface, i.e., provide the ocean forcing [Portabella and Stoffelen, 2009]. Hence, in contrast with NWP, air-sea fluxes of momentum and heat can be accurately determined from scatterometer data [Kelly et al., 2001], [Chelton and Freilich, 2005], and in highly energetic oceanic regions like the western boundary current systems, the ocean currents and mesoscale eddies are accounted for. Furthermore, [Chelton and Xie, 2010], [Vogelzang et al, 2011], [Vogelzang et al, 2015] established that while the effective resolution of scatterometer winds is about 25 km, that of the global NWP winds is about 100-200 km (i.e., the latter are unable to properly resolve small-scale wind variability).

The NWP output therefore misses relevant ocean-atmosphere interaction at both large scales and at the oceanic mesoscale. In line with the latter, [Chelton et al., 2004] filter and find persistent mesoscale features in scatterometer winds (i.e., 4-year averages of 25-km QuikSCAT winds) that are missing in the model wind fields. In addition, [Belmonte-Rivas and Stoffelen, 2019] describe the large-scale circulation NWP errors in ERA5. These persistent features give rise to systematic differences between scatterometer and NWP sea surface winds that have been monitored since the launch of the European Remote Sensing Satellite (ERS-1) in 1991 [Hersbach, 2010]. Such systematic differences are hereafter referred to as local biases that

persist over time, and are visible when scatterometer and model winds are collocated. They mostly represent unresolved geophysical processes by NWP models.

In light of this, attempts to combine scatterometer measurements and NWP estimates (in blended products and data assimilation) allow for increased temporal resolution products, but are affected by the spatial characteristics and caveats of the NWP models, as noted above. In particular, blending products representing different spatial scales, different geophysical processes and with systematic biases in geophysical variables and/or large-scale circulation errors, will result in a blended product with rather artificial and mixed spatiotemporal characteristics, depending on where the satellite measures, where the gaps are and how the local transient weather evolves. The currently most advanced method of blending consists in NWP data assimilation, though also here fundamental issues arise. A main problem is that NWP data assimilation uses the so-called BLUE paradigm, denoting Best Linear Unbiased Estimation, where the existence of biases as noted above obviously conflicts with this paradigm [Stoffelen and Vogelzang, 2018]. Also relevant, NWP model biases in large-scale circulation and parameterizations are restored within a few time steps of model integration after the initialization (analysis step). Therefore, the short-range forecast corrections as proposed in this work do not much depend on whether scatterometer winds are assimilated or not.

In WOC, a new ocean wind forcing product, ERA*, is developed. ERA* consists of a scatterometer-based correction (SC) of the mentioned systematic and persistent effects present in the ERA5 output. The rationale of this method is that when the scatterometer wind data are accumulated over short periods of time, it is possible to overcome sampling errors and maintain some of the scatterometers most beneficial features, i.e., those related to relatively small-scale ocean processes, such as wind-current interaction, and furthermore, correct the large-scale NWP parameterization and dynamical errors. At the same time, the variability over the accumulation time due to fast processes, such as the variability due to moist convection and other transient errors is removed. This is, the ERA* would compute the accurately observed local mean differences to wind scatterometers over a few days. A running mean would reassure the time and space coverage of the original ERA5 atmospheric model fields. With this approach, a scatterometer-based correction, using accurate, unbiased, high spatial resolution ocean vector winds from a combination of several scatterometers, i.e., the Advanced Scatterometer (ASCAT) on board Metop satellites, and/or the OSCAT/OSCAT2 scatterometers on board Oceansat-2/SCATSat-1, is developed. The ERA* approach was initially developed by [Trindade et al. 2020] to correct for ERA-Interim local biases over a few months in 2013, and is applied here to ERA5 and for a longer period of time, i.e., 2010-2020.

2.1 Overview

A general description of the ERA* processor is shown in Fig. 1. The main processing steps consist of:

- Generation of the ERA5 U10S forecasts and scatterometer/ERA5 collocations in a 0.125-deg regular grid (RG)
- Generation of the scatterometer-ERA5 accumulated differences over a specified temporal window, centered around each the UTC time of each ERA5 forecast file

- Generation of the ERA* U10S and wind stress product
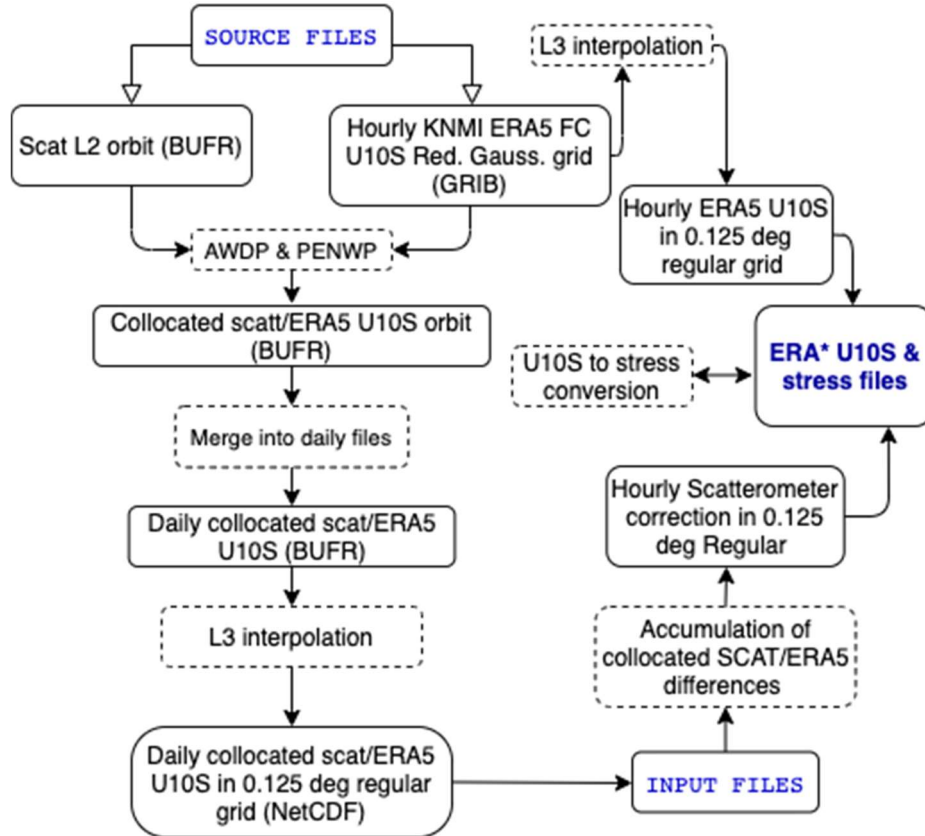
Figure 1.   Schematic illustration of the ERA* processing

2.2 Generation of regular grid data

As shown in Fig. 1, the first step of the ERA* processor is to generate regular grid data from the source files, i.e., the ERA5 hourly forecast (FC) Reduced Gaussian gridded GRIB files at ~31 km (N320, 320 grid points between equator and pole) and the scatterometer Level 2 (L2) swath gridded orbit BUFR files at 12.5-km & 25-km resolution. Note that a combination of the following scatterometers has been used in the generation of the ERA* product for the period 2010-2020: the Advanced scatterometers on board the Metop satellite series (ASCAT-A, ASCAT-B, and ASCAT-C) and/or the scatterometers on board the ISRO Oceansat-2 (OSCAT) and SCATSat-1 (OSCAT2) satellites.

2.2.1 Scatterometer data reprocessing

Although not part of the ERA* processor, note that to improve sensor inter-calibration, the latest versions of the EUMETSAT Ocean and Sea Ice Satellite Application Facilities (OSI SAF) ASCAT

World Ocean Circulation
Project Management Plan

Ref.: WOC-ESA-ODL-NR-
009_T1_ERAstar
Date: 30/06/2022
Issue: 2.0

Wind Data Processor (AWDP) [Verhoef et al., 2020] and Pencil-beam Wind Processor (PenWP) [Verhoef et al., 2018] have been used to reprocess the C-band ASCATs and the Ku-band OSCAT2, respectively. Also note that the latest version of the C-band (CMOD7) and Ku-band (NSCAT4DS) Geophysical Model Functions (GMFs) have been used to retrieve ASCAT and OSCAT2 U10S, respectively. The ERA5 U10S FC data have been used as background for ambiguity removal purposes. The ERA5 10-m equivalent neutral wind (U10N) model output has been retrieved from the ECMWF MARS archive and then converted to U10S by KNMI, using the U10N-to-U10S conversion in [De Kloe et al., 2017]. The reason for converting ERA5 wind output into U10S is to make ERA5 output more compatible with scatterometer retrievals, which have been recently re-defined as U10S [De Kloe et al., 2017] as follows:

$$U10S = U10N \sqrt{\frac{\rho_{air}}{<\rho_{air}>}} \tag{1}$$

where ρ_{air} is the local air density, and $<\rho_{air}>$ the average global air density taken as 1.225 kg/m^3.

The Ku-band HY-2A (HSCAT-A), HY-2B (HSCAT-B), and Rapidscat scatterometer data have also been reprocessed with the latest PenWP version and used for validation purposes in Section 2.4. Note also that the scatterometer data are reprocessed at 12.5-km (ASCATs) and 25-km (OSCATs, HSCATs, and Rapidscat) spatial resolution.

2.2.2 Scatterometer/ERA5 collocations

The OSI SAF scatterometer L2 BUFR files already contain collocated NWP model output data. In our case, since we have reprocessed all scatterometer data with the ERA5 U10S data as background, the scatterometer/ERA5 collocations are already present in the L2 orbit files. In case operational scatterometer L2 data are used as source files, one can collocate the ERA5 U10S GRIB files to the scatterometer data by running AWDP and/or PenWP with the following options:

AWDP: awdp_run -f file1 -nwpfl file2 -noinv -noamb -verbosity 1
PENWP: penwp_run -f file1 -nwpfl file2 -noinv -noamb -verbosity 1

Where "file1" refers to the scatterometer file and "file2" to the filelist containing the ERA5 forecast GRIB files to be spatially and temporally interpolated to the scatterometer swath. To kip the scatterometer wind retrieval process, the options "noinv" and "noamb" are set.

Then the scatterometer L2 orbit files (containing ERA5 U10S collocated data) are merged into daily files.

World Ocean Circulation
Project Management Plan

Ref.: WOC-ESA-ODL-NR-
009_T1_ERAstar
Date: 30/06/2022
Issue: 2.0

2.2.3 L3 interpolation

Both the daily scatterometer/ERA5 swath-gridded files and the hourly ERA5 U10S forecast Reduced Gaussian grid files are then interpolated to a level 3 (L3) regular grid (RG) of 0.125 deg resolution. An adaptation of the CMEMS L3 interpolation tool [Driesenaar et al., 2020] is used to produce daily L3 maps of collocated scatterometer/ERA5 U10S. While the CMEMS tool produces daily maps of non-overlapping scatterometer orbits, here we produce daily maps of the full scatterometer coverage (accounting for overlaps). Both the daily collocated scatterometer/ERA5 U10S fields and the hourly ERA5 U10S forecast fields are produced in NetCDF format.

2.3 Generation of scatterometer corrections

As in [Trindade et al., 2020], the scatterometer-based correction (*SC*) to produce ERA* is applied to both the zonal and the meridional U10S components (u_{10s}, v_{10s}). Note that since the same formulation is used to correct the biases in both U10S components, for simplicity, only the zonal component equations are shown in this Section.

The correction is based on the temporally averaged difference between scatterometer (u_{10s}^{SCAT}) and ERA5 U10S (u_{10s}^{ERA5}), at grid point (*i,j*) and time sample (*t*), as described in the following equation:

$$SC(i,j,t_f) = \frac{1}{M}\sum_{t=1}^{M}\left(u_{10s}^{SCAT_k}(i,j,t) - u_{10s}^{ERA5}(i,j,t)\right) \qquad (2)$$

Here, $u_{10s}^{SCA\ k}$ and u_{10s}^{ERA5}, respectively, correspond to the collocated scatterometer/ERA5 zonal U10S component, in which k refers to the number of sensors used in the *SC*. The data sets are collocated for a temporal window of *N* days, centered at t_f, i.e., $t_f \pm N/2$ days, where *M* is the number of scatterometer/ERA5 collocations at grid point (*i,j*) within the defined time window around the ERA5 forecast time t_f.

As such, for each t_f and fixed temporal window configuration (N), the collocated scatterometer/ERA5 fields (Section 2.2.3) within $t_f \pm N/2$ days are collected and the corresponding scatterometer/ERA5 differences averaged at each grid point (2). This leads to the generation of hourly (at each t_f) SC U10S fields for a predefined time window (N) and combination of scatterometers (*k*).

To efficiently reduce NWP local biases, a trade-off between optimal scatterometer sampling and the ability to keep the small spatial and temporal ocean induced scales is required. The scatterometer sampling characteristics have a large impact on the effectiveness of this method.

World Ocean Circulation
Project Management Plan

Ref.: WOC-ESA-ODL-NR-
009_T1_ERAstar
Date: 30/06/2022
Issue: 2.0

A relevant limitation is that scatterometer spatial sampling is non-uniform, i.e., it varies with both the latitude and the longitude, resulting in reduced coverage over the tropics when compared to other latitudes. Still, in-time accumulation of data from the different scatterometers allows for a significant reduction in revisit time [Tang et al., 2014]. Additionally, ERA5 local biases are relatively persistent over time but such persistence is also regionally dependent, e.g., is longer in the trades than in rest of the tropics and higher latitudes. As such, the ERA* processor allows several configurations, with different temporal windows and varying number of scatterometers, which will be tested in Section 2.5 to find the best quality general ocean forcing product.

In particular, *k* refers to different combinations of the available scatterometers over the 2010-2020 period, which include the C-band ASCATs (A, B, C) and the Ku-band OSCAT and OSCAT2. Further details are provided in Tables 1 and 2.

Regarding the temporal window (N) for the SC, several configurations are tested, i.e., $N = 1, 3, 5, 10, 15, 30$ days. In contrast with [Trindade et al., 2020], for WOC SC temporal windows longer than 5 days are tested. This is done to check the temporal persistence of the local biases assumed in ERA5 U10S fields. While for longer time windows, a larger scatterometer sampling is achieved, the performance of ERA* will rely on the persistence of such systematic errors. As such, the trade-off between sampling and local bias persistence is further analyzed with longer temporal windows.

2.4 Generation of ERA*

Finally, the scatterometer correction, $SC(i, j, t_f)$, is added to the ERA5 U10S forecasts, $u_{10s}^{ERA5}(i, j, t_f)$ at time t_f as follows

$$u_{10s}^{ERA*}(i, j, t_f) = u_{10s}^{ERA5}(i, j, t_f) + SC(i, j, t_f) \tag{3}$$

The ocean forcing product derived from (3), u_{10s}^{ERA*}, has a grid resolution of 0.125 deg and temporal resolution of 1 h, following ERA5.

Finally, both the ERA5* and ERA5 FC U10S fields are converted to wind stress by applying the following standard formula:

$$\tau = C_{D10} < \rho_{air} > |U_{10}| U_{10S} \tag{4}$$

In which we use a standard average air density value for of 1.225 kg/m3 and a drag coefficient which is determined from the ERA Interim by fitting a line to a full year of data (see Fig. 18 in [De Kloe et al., 2017]). The resulting line is characterized by the following equation:

$$C_{D10}(U_{10}) = aU_{10} + b \tag{5}$$

World Ocean Circulation
Project Management Plan

Ref.: WOC-ESA-ODL-NR-
009_T1_ERAstar
Date: 30/06/2022
Issue: 2.0

in which, $a = 7.94x10^{-5}$ and $b = 6.12x10^{-4}$

This is very close to the relation used by the Coare3.5 (Edson et al, 2013) parameterization. The function defined above is used to convert both the scatterometer and the model U10S to stress. Constant values are used instead of model values for the air density and drag coefficient parameters to avoid any dependence of the scatterometer stress on a particular model.

Given the validation results in Section 2.5, where the performance of ERA* is assessed using buoy and independent scatterometer U10S as reference, the optimal ERA* configuration in terms of accuracy and resolution is $k = 4$ and $N = 3$ [Portabella et al., 2021], which means that in (2) u_{10}^{SCATk} includes measurements from 4 different sensors, i.e., ASCAT-A, -B, and -C, and OSCAT2 and SC is computed over a 3-day temporal window. However, in periods when this optimal combination of one or several ASCATs and one OSCAT is not available, e.g., periods when OSCAT or OSCAT2 were not in orbit (2014-2016) or were operating but suffered long data interruptions (2010-2012, 2017, and 2019), the ERA* data quality is substantially degraded when using the 3-day temporal window, and a longer temporal window of 15 days is needed to achieve a significantly better U10S quality than that of ERA5 (see sections 2.5.4 and 2.5.5). Moreover, in 2010, when only ASCAT-A and OSCAT data were available, because of the OSCAT long data interruptions (more than 3 months), a temporal window of 30 days is required to ensure good data quality. The notation for the different ERA* configurations tested can be found in Table 1. Note that since OSCAT and OSCAT2 do not overlap in time, the same label "O" has been used for simplicity.

Table 1. Notation for the different ERA* configurations according to the combination of sensors and temporal window used.

Data Source \ Temporal Window	N1	N3	N5	N10	N15	N30
ASCAT-A	ERA*$_A$N1	ERA*$_A$N3	ERA*$_A$N5	ERA*$_A$N10	ERA*$_A$N15	ERA*$_A$N30
ASCAT-A, ASCAT-B	ERA*$_{AB}$N1	ERA*$_{AB}$N3	ERA*$_{AB}$N5	ERA*$_{AB}$N10	ERA*$_{AB}$N15	ERA*$_{AB}$N30
ASCAT-A, ASCAT-B, ASCAT-C	ERA*$_{ABC}$N1	ERA*$_{ABC}$N3	ERA*$_{ABC}$N5	ERA*$_{ABC}$N10	ERA*$_{ABC}$N15	ERA*$_{ABC}$N30
ASCAT-A, OSCAT	ERA*$_{AO}$N1	ERA*$_{AO}$N3	ERA*$_{AO}$N5	ERA*$_{AO}$N10	ERA*$_{AO}$N15	ERA*$_{AO}$N30
ASCAT-A, ASCAT-B, OSCAT	ERA*$_{ABO}$N1	ERA*$_{ABO}$N3	ERA*$_{ABO}$N5	ERA*$_{ABO}$N10	ERA*$_{ABO}$N15	ERA*$_{ABO}$N30
ASCAT-A, ASCAT-B, ASCAT-C, OSCAT	ERA*$_{ABCO}$N1	ERA*$_{ABCO}$N3	ERA*$_{ABCO}$N5	ERA*$_{ABCO}$N10	ERA*$_{ABCO}$N15	ERA*$_{ABCO}$N30

2.5 Product validation

In this section, a comprehensive characterization of the ERA* U10S product is presented. The year 2019 is used as testbed for such characterization, since this period contains the largest scatterometer constellation, thus allowing to test the performance of different scatterometer combinations. A qualitative comparison between the ERA5 and ERA* products is shown in section 2.5.1. Then, the U10S quality is assessed against independent scatterometer observations (i.e., HSCAT-B) in section 2.5.2, and the geophysical consistency of the derived maps is assessed through spectral analysis in section 2.5.3. In section 2.5.4, an assessment of the different ERA* configurations for a varying scatterometer constellation is carried out with the 2019 dataset, using both buoy and independent HSCAT-B U10S data. Section 2.5.5 provides a thorough

World Ocean Circulation
Project Management Plan

Ref.: WOC-ESA-ODL-NR-
009_T1_ERAstar
Date: 30/06/2022
Issue: 2.0

analysis of the impact of scatterometer data gaps on the ERA* product performance. Finally, the selected period-dependent ERA* configurations are thoroughly assessed using independent scatterometer (HSCATs and Rapidscat) data for several years within the 2010-2020 period.

Note that the same U10S-to-stress conversion is applied to all the products (ERA5, ERA*, and HSCAT-B). As such, there is no need to present a verification of the ERA* stress product per se.

2.5.1 Systematic local differences

Local systematic differences between collocated scatterometer and ERA5 are generally within $\pm 2 m.s^{-1}$, see Fig. 2. These differences are most noticeable where physical processes are misrepresented or absent in the model, therefore very pronounced over the western boundary ocean current systems (WBCS, i.e., the Agulhas current, the Gulf Stream or the Kuroshio current), the Antarctic Circumpolar Current (ACC), and in adjacent regions where the eddies generated by these currents detach. Likewise, in the tropics (see, e.g., the Inter Tropical Convergence Zone or ITCZ), U10S differences (particularly in the meridional component in Fig. 2b) are notable where the model U10S field is unable to capture both the detailed and large-scale wind circulation.

Local wind effects like see breeze, katabatic flows, corner winds or wind funneling effects (gap winds) are also visible in Fig. 2. The latter are readily evident from the meridional component in Fig. 2b, e.g., see the gap wind effect in the Gulf of Tehuantepec (Central America, south of Mexico). Apart from the increase in wind speed, gap winds also strengthen tidal currents, furthermore affecting ocean circulation.

Fig. 3 shows an ERA5 U10S global map (a) and its corresponding ERA* (b) generated with a four-scatterometer based correction (i.e., ASCAT-A, -B, -C, and OSCAT2) over a three-day temporal window ($ERA*_{ABCO} N3$). By simply comparing ERA5 and $ERA*_{ABCO} N3$ U10S global maps, it is clear that both contain very similar structures, as expected, since the ERA* does not aim at correcting transient weather effects but local systematic effects. $ERA*_{ABCO} N3$ contains additional small-scale variance when compared with ERA5 (Fig. 3a is smoother than Fig. 3b), notably at the same locations where larger local biases emerge in Fig. 2b, although this is difficult to appreciate in a global map. In this line, Fig. 3a differs from Fig. 3b in that the increased variability seen in the latter should better capture the stationary signal from WBCS, the wind shadowing effects in the vicinity of islands, and the coastal effects associated to coastal orography.

World Ocean Circulation
Project Management Plan

Ref.: WOC-ESA-ODL-NR-
009_T1_ERAstar
Date: 30/06/2022
Issue: 2.0
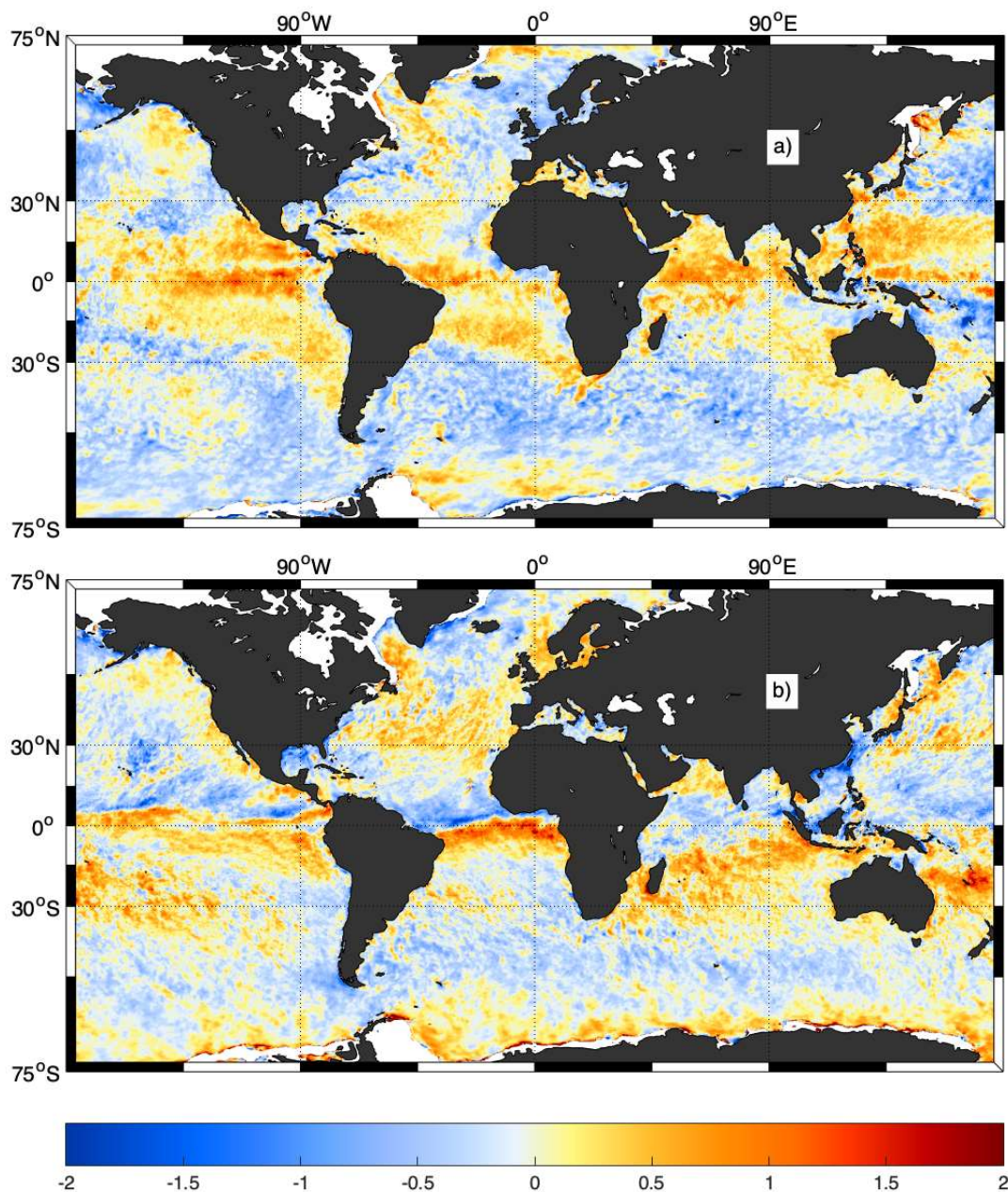
Figure 2. Scatterometer Correction (SC) for a given day, i.e., 15th of February 2019. Collocated differences between ASCAT-A/B/C and ERA5 U10S for the zonal (a) and the meridional (b) wind components, accumulated over a 30-day temporal window centered around 09 UTC. The colors represent the differences in $m.s^{-1}$ (see color scale).

World Ocean Circulation
Project Management Plan

Ref.: WOC-ESA-ODL-NR-
009_T1_ERAstar
Date: 30/06/2022
Issue: 2.0

To discern the difference in small scale variance between the two maps in Fig. 3, a zoom over the tropical Atlantic region is shown in Fig. 4 (which corresponds to the red box in Fig. 3). Additionally, Fig. 4c shows the same map for another ERA* product generated with a shorter temporal window of one day ($ERA*_{ABCO}N1$). Fig. 4b arguably shows moist convection induced variability south of the West African coast, clearly visible in the $ERA*_{ABCO}N3$, but not in the ERA5 (Fig. 4a). The $ERA*_{ABCO}N1$ map (Fig. 4c) shows even larger variability than the $ERA*_{ABCO}N3$ map (Fig. 4b). The use of a longer temporal window in $ERA*_{ABCO}N3$ than in $ERA*_{ABCO}N1$ is responsible for the additional smoothing of the wind fields of the former, but also for the reduction of scatterometer weather sampling errors. This probably indicates that the $ERA*_{ABCO}N1$ map (Fig. 4c) captures small-scale variability associated with relatively fast evolving atmospheric phenomena, while the $ERA*_{ABCO}N3$ map (Fig. 4b) does not.

Note also that this increased variability is attributed to moist convection, because it can be depicted by the scatterometers (due to updrafts and downdraft), in agreement with the findings of [Lin et al., 2015a], [Lin et al., 2015b], [King et al., 2017] over the tropical band. Although moist convection impacts the ocean exchange processes of momentum, heat and moisture and is fundamental to ocean model forcing, it cannot be fully resolved using a static mean correction, since the SC likely misses the highly variable component in moist convection (wind changes up to 15 m/s over a 30 min window). Due to the fast weather evolution during a satellite orbit, $ERA*_{ABCO}N1$ clearly shows some small-amplitude "jumps" or artifacts (see, e.g., several straight lines in the top-left quadrant of Fig. 4c), which are not visible in the $ERA*_{ABCO}N3$ (Fig. 4b), which smooths weather effects over 3 days. Such artifacts are associated with the edges of the different scatterometer swaths used, indicating that the 1-day corrections (N1) are based on relatively poor scatterometer weather sampling at these latitudes. Moreover, although such jumps may be small, they certainly become more evident in wind derivative products, such as divergence or curl (not shown).

Additional variance, as seen in these regional maps of the ERA* meridional U10S component, manifests alike in all the ERA* configurations in Table 1 and in the U10S zonal component (not shown), indicative of persistent mesoscale (ocean) variability. A more quantitative validation is presented in the next sections in order to verify and complete the preliminary conclusions drawn from the qualitative comparison presented in this section.

World Ocean Circulation
Project Management Plan

Ref.: WOC-ESA-ODL-NR-
009_T1_ERAstar
Date: 30/06/2022
Issue: 2.0
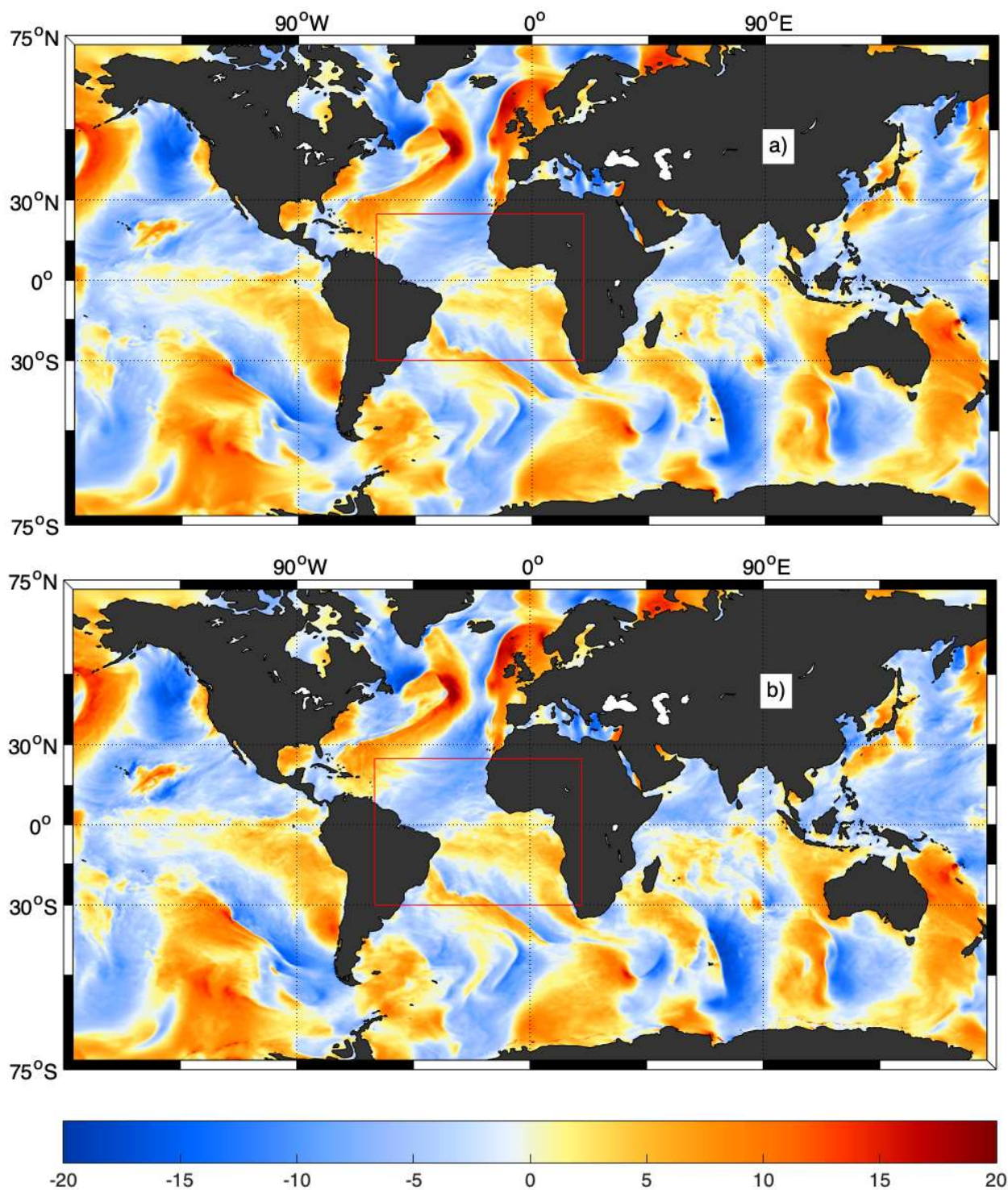
Figure 3.   U10S meridional component for ERA5 (a) and ERA* on the 15th of February 2019 at 09 UTC. The ERA* map is based on ASCAT-A, ASCAT-B, ASCAT-C, and OSCAT2 corrections over a 3-day temporal window. The red box indicates the area shown in Fig. 4.

World Ocean Circulation
Project Management Plan

Ref.: WOC-ESA-ODL-NR-
009_T1_ERAstar
Date: 30/06/2022
Issue: 2.0
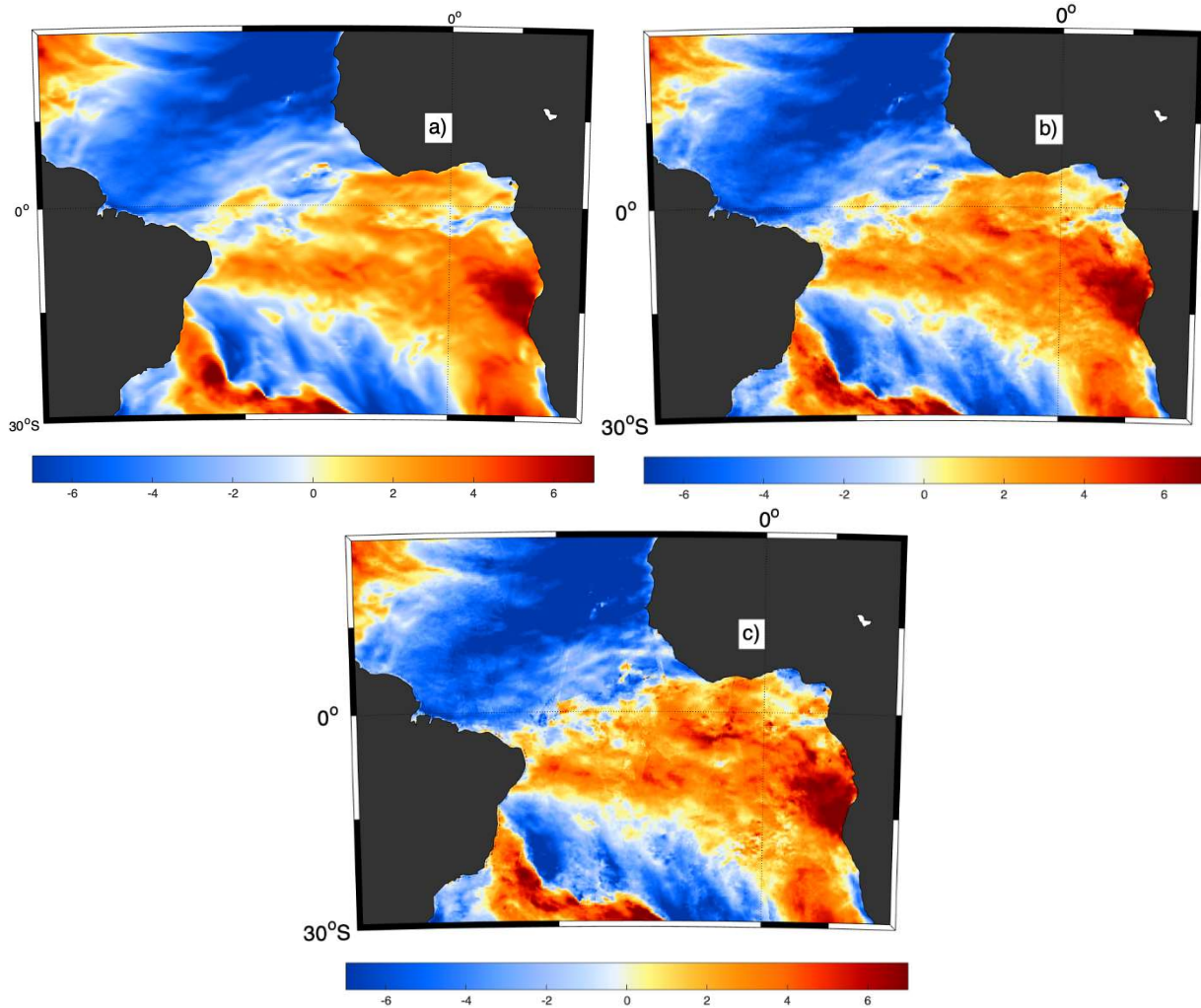
Figure 4.   U10S meridional component over the West African coast for the ERA5 and ERA* products shown in Fig. 3 (see red box). The ERA* shown in (c) is the same as that of (b) but for a SC over a 1-day temporal window (N1). The winds are truncated beyond [-7, 7] $m.s^{-1}$ to better highlight the differences between the three maps.

2.5.2 Verification against HSCAT-B

In the previous section, a qualitative assessment of ERA* U10S maps reveals enhanced variability with respect to the original ERA5 U10S. In this section we check whether this additional variance is dominated by true wind signal rather than noise, by assessing the quality of the different ERA* configurations (see Table 1) against independent HSCAT-B U10S data.

HSCAT-B is a good wind reference since the orbit pass (6 am/6 pm) is very different from that of the instruments used to correct the ERA5 fields, i.e., ASCAT-A/B/C at 9:30 am/9:30 pm and OSCAT2 at 8:45 am/8:45 pm. The use of ASCAT-A/B/C and OSCAT2 together substantially

increases the local sampling, but is insufficient to fully capture the diurnal cycle as these sensors sample the same location of the ocean with only a 45 min difference. However, if the model diurnal cycle is reasonable and local biases are persistent over longer periods (6-12 hours), then the scatterometer-based corrections would lead to a reduction of model errors at HSCAT-B verification times, which are 3:30 and 2:45 hours apart from ASCAT-A/B/C and OSCAT2, respectively. Furthermore, if these local biases are persistent over several days, then the ERA* product generated with a larger temporal window (of several days) would be of higher quality than that generated with a one-day temporal window, since the former has a better downsampling of the mesoscale weather variability than the latter.
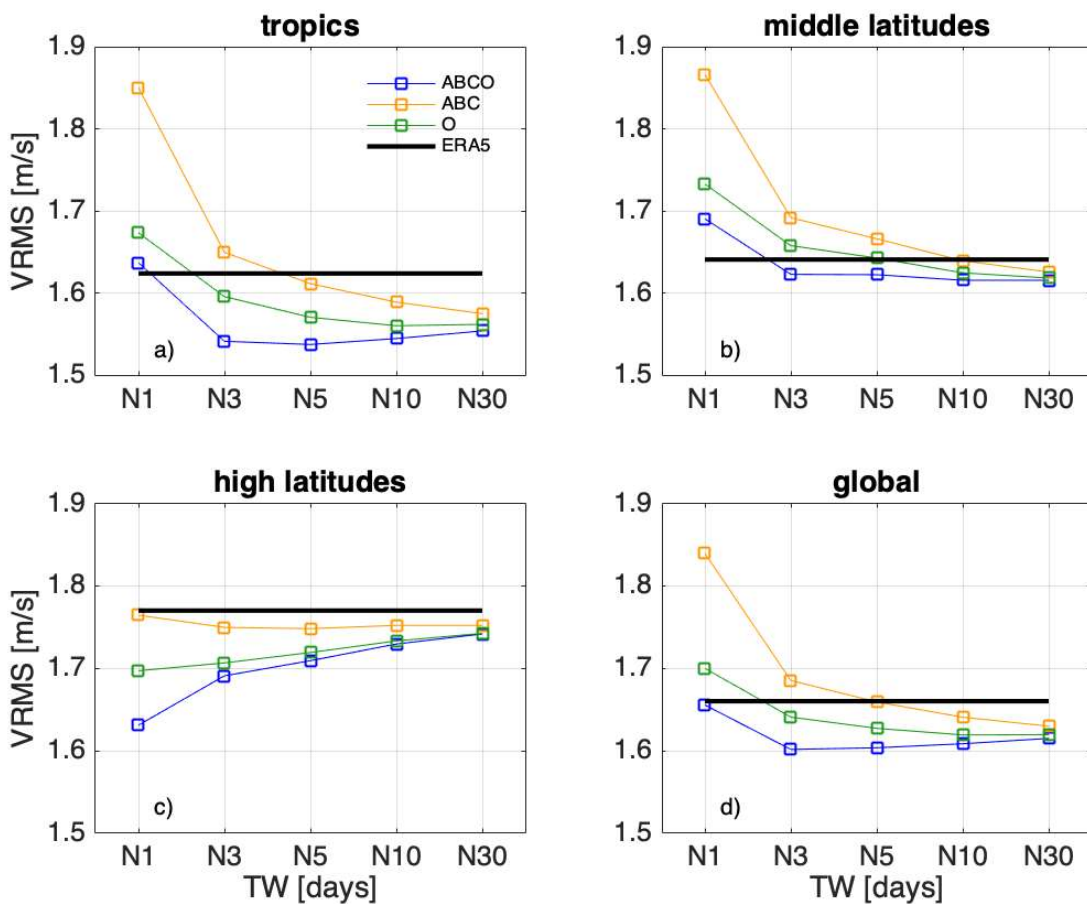
Figure 5. Estimated Vector root mean square (VRMS in ms^{-1}) difference between different ERA5/ERA* U10S products and HSCAT-B U10S as a function of the SC temporal window size, over a month period (February 2019), for the tropics (a), middle latitudes (b), high latitudes (c), and the global ocean (d). The different colour lines show the VRMS scores for ERA5 (black line in bold), ERA* configuration using ASCAT-A/B/C (orange), ERA* using OSCAT2 (green), and ERA* using ASCAT-A/B/C and OSCAT2 (blue). The colored curves below the horizontal black line indicate the different ERA* configurations that outperform ERA5.

Fig. 5 shows the vector root-mean-square difference (VRMS) between the different ERA* configurations (see legend) and HSCAT-B U10S as a function of the temporal window size (in days), for the tropics (top left), the middle latitudes (top right), the high latitudes (bottom left) and global (bottom right). For reference, the VRMS between ERA5 and HSCAT-B is plotted with a thick black solid horizontal line. The latter is used as benchmark, i.e., only those ERA* configurations below the black line are of higher quality (with respect to HSCAT-B) than ERA5. The different geographical regions are defined as: 30S-30N (tropics); 30S-55S & 30N-55N (middle latitudes); and beyond 55S & 55N (high latitudes).

Except for high-latitude regions, all ERA* configurations, i.e., $ERA*_{ABC}$ (yellow curves), $ERA*_O$ (green curves), and $ERA*_{ABCO}$ (blue curves) show an improved performance with temporal wind size, notably for shorter windows. $ERA*_{ABC}$ and $ERA*_O$ show best performance at long temporal windows (more than 10 days), indicating that the weather downsampling of scatterometer data over short periods of time is rather poor and therefore a larger temporal window is required to reduce the model weather errors. Note the abrupt drop in VRMS that occurs if the ERA* is generated with a correction based on up to three days of accumulated scatterometer information. In particular, a 3-5 days window (N3 or N5) is needed to outperform ERA5.

As expected, when adding all available scatterometers ($ERA*_{ABCO}$), the model weather errors are considerably reduced at short temporal windows. In particular, when complementary scatterometer orbits are used in the corrections, the derived ERA* products (see blue curves in Fig. 5) outperform ERA5 at N3 in all the regions. In fact, for $ERA*_{ABCO}$ configurations, the quality of the data does not significantly depend on the temporal window size when longer than N3. In fact, the quality of the ERA* product slightly degrades for N5-N30 (see e.g., blue curve on Fig 5d). This is probably due to a compensation effect: on the one hand, the larger the temporal window, the larger is the sampling; on the other hand, the larger the temporal window, the more sensitive the system is to local bias changes.

Also note that when comparing ERA5 quality (black solid line) against that of $ERA*_{ABCO}$ (blue curve) for the tropics (Fig. 5a) and the middle latitudes (Fig. 5b), the ERA* outperformance w.r.t ERA5 is much larger in the tropics. In particular, ERA* has around 10% lower error variance (VRMS[2]) than ERA5 in the tropics, while only 2.5% lower in the middle latitudes. As shown in [Trindade et al., 2020], the mid-latitude local biases seem to be less persistent than those in the tropics. This may be caused by the impact of fast evolving weather not well captured by ERA5, e.g., mislocation of mid-latitude synoptic variability.

Another reason for this relatively lower ERA* performance in the middle latitudes is the presence of residual biases in the OSCAT2 U10S as a function of the across-track location [Wang et al., 2019]. Since the OSCAT2 orbit has a repeat cycle of 2 days (29 orbits), the mentioned biases have a geographical pattern (not shown), which could directly impact the effectiveness of the proposed ERA* method that lies under the assumption of well intercalibrated scatterometer data sets, i.e., the better the C-band and Ku-band systems are intercalibrated, the better the ERA* performance is. Within CMEMS, current efforts are devoted to reduce such Ku-band system biases. Should this be achieved, the ERA* performance is expected to significantly improve in the future.

Also relevant are the relatively lower VRMS scores for $ERA*_O$ than for $ERA*_{ABC}$, when the latter contains substantially larger scatterometer sampling than the former. The reason for this is that

both the OSCAT2 U10S and the HSCAT-B U10S used for verification are Ku-band systems. As shown in [Vogelzang et al., 2011], rotating pencil-beam Ku-band systems are noisier than the fixed fan beam C-band ASCATs. A variational approach is used to reduce such additional noise, which in turn filters small-scale signal [Portabella and Stoffelen, 2004]. In consequence, Ku-band U10S fields are smoother (lower resolution) than C-band U10S. This may indeed lead to the lower VRMS scores for $ERA *_O$, as compared to those for $ERA *_{ABC}$. Interestingly, the addition of ASCAT-A/B/C and OSCAT2 sampling ($ERA *_{ABCO}$) leads to the lowest scores, which is consistent with the expected effect of the scatterometer sampling on ERA* performance.

At high latitudes, i.e., above 55N and below 55S, the abundant (sun-synchronous) satellite sampling is expected to be optimal to model local bias reduction. However, a dedicated study is required to appropriately account for SST and the seasonality of the sea ice extent and its impact on the scatterometer wind-retrieval errors, quality control, and sampling. Moreover, the dynamical weather errors are more transient at high latitudes, probably resulting in a different optimum averaging period. Fig. 5c indeed shows the best performance at N1 rather than N3, indicating the relatively larger scatterometer sampling and more transient weather effects in this ocean region as compared with lower latitude regions. Other seasons and years though show the lowest scores at N3 (not shown), indicating indeed sea ice seasonality effects.
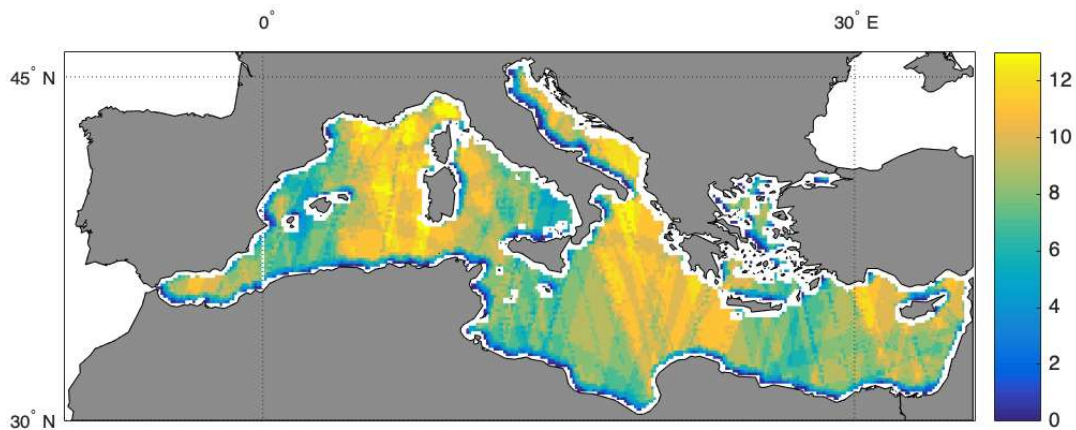
Figure 6. Combined ASCAT-A/B/C and OSCAT2 sampling pattern for a 3-day temporal window in the Mediterranean Sea.

The quality of ERA* in coastal regions is also assessed. Increased wind variability conditions, including relatively steep wind gradients, are expected near the coast. Moreover, the scatterometer sampling is rather irregular and poor along the coastline, as compared with open ocean grid points. Fig. 6 shows the 3-day scatterometer sampling pattern in the Mediterranean, for the combined ASCAT-A/B/C and OSCAT2 scatterometers. A substantial decrease in the scatterometer sampling can be seen along the closest grid points to the coast. Despite the decreased scatterometer sampling, a similar ERA* performance behavior is found at the coast (Fig. 7), as compared to other ocean regions (Fig. 5). Once again, the $ERA *_{ABCO}$ N3 configuration shows the lowest VRMS scores and significantly outperforms ERA5 U10S.

World Ocean Circulation
Project Management Plan

Ref.: WOC-ESA-ODL-NR-
009_T1_ERAstar
Date: 30/06/2022
Issue: 2.0
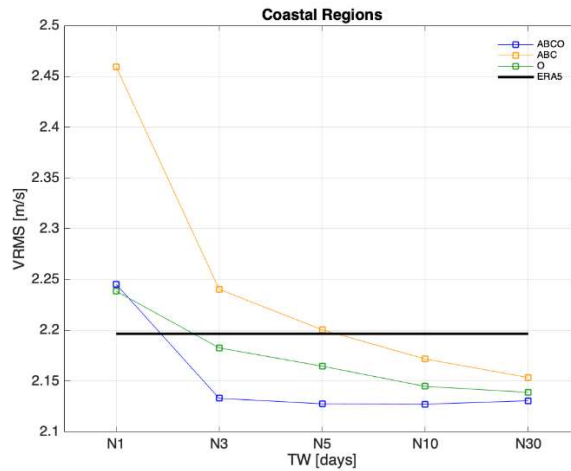
Figure 7.   Same as Fig. 5, but for coastal regions only.

Finally, the effects of transient weather on the ERA* product quality is preliminarily assessed. As already mentioned, the ERA* methodology does not aim at correcting for transient weather effects but for local systematic effects. The latter effects are of the order of about $\pm 2ms^{-1}$. Fig. 8 shows the distribution of SC values for a temporal window of 3 days and the combination of ASCATs and OSCAT2 (i.e., ABCO). It is clear that there are outliers in the distribution (see tails of the distribution exceeding by far the expected local systematic effects), which appear due to transient weather effects (e.g., storm phase shifts in ERA5, mislocation of fronts, etc.). These are, as expected, more prominent in shorter temporal windows than in longer windows (the lower the sampling, the larger the impact of transient weather in the SC).
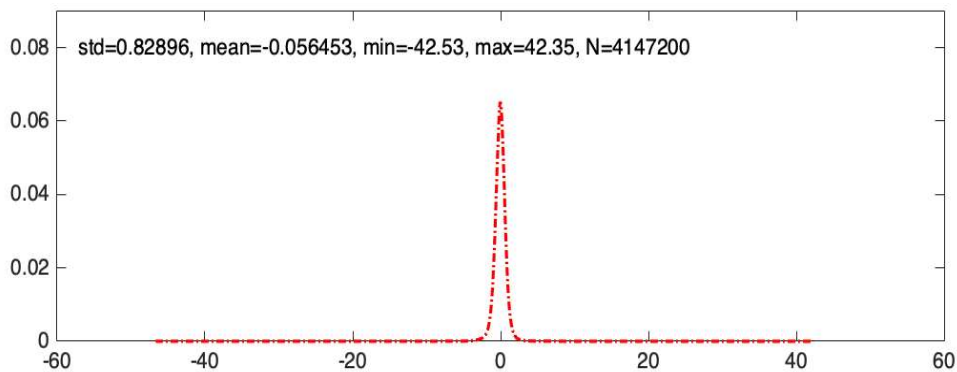
Figure 8.   Normalized histogram of the SC values (2) obtained for a temporal window of 3 days and the combination of ASCATs and OSCAT2 (i.e., ABCO).

As such, the standard deviation (SD) of scatterometer-ERA5 differences is calculated for each scatterometer over a long temporal window (30 days), resulting in the following values: 1.67 m/s and 1.59 m/s (1.27 m/s and 1.33 m/s) for the zonal and meridional U10S component of the ASCATs (OSCAT2), respectively. Then a 3-sigma filter is applied to the individual scatterometer-ERA5 differences before computing the corresponding SC (2). Note that the 3-sigma filter results in a reduction of about 1.3% of the scatterometer sampling. The resulting ERA* product (3) is then verified again against HSCAT-B. Fig. 9 shows the VRMS scores between two different ERA*

configurations ($ERA*_{ABCO}$ and the same configuration but with the 3-sigma test applied) and HSCAT-B U10S as a function of the temporal window size, for the same four regions defined in Fig. 5. Indeed, this preliminary test on outlier removal seems quite effective, as $ERA*_{ABCO}$ with 3-sima test overperforms $ERA*_{ABCO}$ for short temporal windows. In particular, $ERA*_{ABCO}$N3 with 3-sigma test has in general the lowest VRMS scores, showing an error variance (VRMS[2]) reduction w.r.t. ERA5 of about 9% globally, ranging from about 5% reduction in the middle latitudes to 12.5% reduction in the tropics.
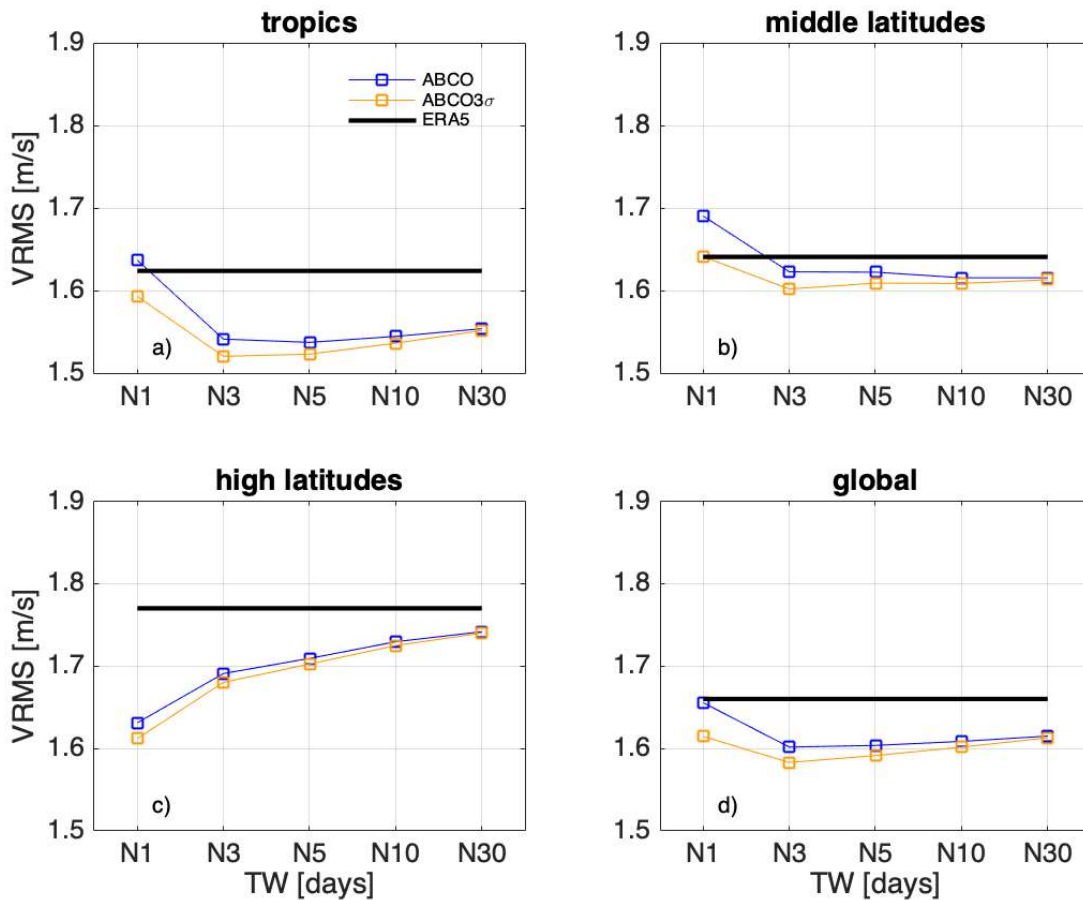
Figure 9. Same as Fig. 5, but for $ERA*_{ABCO}$ (blue) and $ERA*_{ABCO}$ with 3-sigma test (orange).

2.5.3 U10S spectra

The verification against independent scatterometer data presented in the previous section shows a significant reduction of model errors, in particular when complementary scatterometer data are used to correct the U10S in the tropics, high latitudes and coastal regions. These findings support that overall most of the high frequency signal observed in the qualitative assessment of the derived ERA* maps (discussed in section 2.5.1) is dominated by true ocean-related wind signal rather than by noise.

World Ocean Circulation
Project Management Plan

Ref.: WOC-ESA-ODL-NR-
009_T1_ERAstar
Date: 30/06/2022
Issue: 2.0

In this section, the derived ERA* U10S fields are assessed in terms of their geophysical consistency and effective resolution, using spectral analysis. Note that only the results for the meridional U10S component are shown, but similar conclusions can be drawn for the zonal component.

In line with [Vogelzang et al., 2011], to obtain the U10S spectra, valid samples of the U10S components are collected over a month (February 2019) in the HSCAT-B along-track direction for each across-track wind vector cell (WVC). To comply with the assumption of periodicity imposed when using FFT, a linear transformation detrending method is applied to the samples. Fig. 10 shows the final spectra, i.e., the individual spectra averaged over all WVC numbers across the swath and over the mentioned time period. Overall, for HSCAT-B, 1578 (8458) individual spectra were averaged in the tropics (middle latitudes). The substantially larger number of individual spectra used for ASCAT with respect to HSCAT-B is due to the much lower QC rejection rate of C-band systems with respect to that of Ku-band systems [Lin et al., 2015a] [Lin and Portabella, 2017]. Note that the SC field contains both ascending and descending passes and hence many swath edges implied in ERA* cross the HSCAT samples, potentially causing a white noise (flat) spectrum tail when insufficiently sampled.

In particular, this Figure shows the spectra for the meridional U10S component in the tropics (Fig. 10a) and the mid-latitudes (Fig. 10b) for a fixed combination of scatterometers (i.e., ASCAT-A, ASCAT-B, ASCAT-C, and OSCAT2) and for various temporal window sizes (see the last row of Table 1).

The solid lines show the model U10S spectra for the same sample length (128) as those collected for the HSCAT-B data (dashed pink). The red solid line shows the ERA5 spectrum, while the different ERA* configurations (sorted as in the last row of Table 1) are shown in orange, blue, green, purple, and cyan. The black dashed line shows the spectral slope of $k^{-5/3}$ for comparison.

World Ocean Circulation
Project Management Plan

Ref.: WOC-ESA-ODL-NR-
009_T1_ERAstar
Date: 30/06/2022
Issue: 2.0

Figure 10. Power density spectra for the meridional U10S component of HSCAT-B (dashed pink), and collocated ERA5 (red) and ERA* (see colour legend) products, in the tropics (a) and the middle latitudes (b). The ERA* products based on combined ASCAT-A, ASCAT-B, ASCAT-C, and OSCAT2 (ABCO notation) SC for different temporal windows are shown. The $ERA*_{ABCO} N$ notation from N1 to N30 corresponds respectively to SC temporal windows from 1 to 30 days (see Table 1).

Globally, a spectral slope close to $k^{-5/3}$ is reported by [Nastrum and Gage, 1985] for aircraft wind measurements, and by [Vogelzang et al., 2011] [Trindade et al., 2020] for the ASCAT-A 12.5-km U10S product at scales below 500 km, as they follow Kolmogorov 3D turbulent theory of the atmosphere. While a k^{-2} slope is referenced by, e.g., [Chelton et al., 2006], using QuikSCAT winds, i.e., a previously released instrument with a similar design to that of HSCAT-B. Indeed, somewhat steeper slopes were found for HSCAT-A than for ASCAT-A in [Trindade et al., 2020], indicating that the latter is able to resolve smaller scales than the former.

Random atmospheric 3D turbulence has a life cycle of a few hours and therefore it's not likely captured by the SC (longer time windows), and consequently also not by ERA*. However, wind features coupled to the ocean mesoscales will largely remain, as well as systematic ERA5 flow errors, e.g., tied to the slower synoptic weather patterns and large-scale circulation errors [Belmonte-Rivas and Stoffelen, 2019]. As shown by [Reynolds and Chelton, 2010], [Hoareau et

World Ocean Circulation
Project Management Plan

Ref.: WOC-ESA-ODL-NR-
009_T1_ERAstar
Date: 30/06/2022
Issue: 2.0

al, 2018] the spectral slopes for oceanic turbulence tracers such as Sea Surface Temperature (SST) and Sea Surface Salinity (SSS) are typically between -1 and -3. However, whilst both present similar spectral slopes atmospheric turbulence is more energetic (i.e., larger variance) than oceanic turbulence. In that sense, assuming the oceanic turbulence is well captured by the SC (i.e., oceanic features which persist over a few days), one expects gentler slopes in ERA* (i.e., more comparable to those of HSCAT-B or ASCAT winds) than in ERA5. This is in line with the spectral slopes shown in Fig. 10 for and HSCAT (dashed pink). Also, in line with the ECMWF spectra shown in [Vogelzang et al., 2011], the ERA5 spectra present a steep slope at high frequencies, indicating a lack of spatial scales below 100-150 km in the model U10S. Note though that the ERA5 slopes are less steep than those of ERA-Interim (see [Trindade et al., 2020]), indicating that the latter contains somewhat more small-scale variance than the latter.

The spectral slopes observed for the ERA* in Fig. 10 lay between those of ERA5 and HSCAT-B (except for the N1 configuration; see orange curve), indicating that ERA* is able to resolve smaller scales than ERA5 although the U10S fields are somewhat smoother than those of HSCAT-B. Note also that the shorter the temporal window used in ERA*, the closer the ERA* spectral slope is to that of HSCAT-B, i.e., a finer scale ERA* product is obtained showing more sampled 3D turbulence or weather, which is undesirable as noted above. However, following the verification carried out in section 2.5.2, we note that the SC substantially reduce the ERA*/HSCAT-B VRMS differences and hence are associated with persistent biases and not with random 3D atmospheric turbulence. Note though that a slight indication of a flat spectrum tail is noticeable at high frequencies, also noticeable in HSCAT-B (see dashed pink curve in Fig. 10), indicating that a small part of the fast and random $k^{-5/3}$ 3D turbulence and convection is present as noise. Following Fig. 5, we note that better ERA* verification is obtained after 3-5 days.

The dependence of the spectral slope on spatial sampling is analysed in Fig. 11. The spectra for the meridional wind component are displayed for a fixed time window (N3) with different combinations of scatterometers, as listed in the second column of Table 1, alongside HSCAT-B (dashed pink) and ERA5 (solid red) spectra. Note that while $ERA*_O N3$ and $ERA*_{ABCO} N3$ have similar spectral slopes, $ERA*_{ABC} N3$ has a somewhat less steep curve, similar to that of HSCAT-B. Moreover, it contains larger variance at intermediate and small scales than HSCAT-B. This is expected since the ASCATs are of higher resolution than the Ku-band systems like OSCAT-2 [Vogelzang et al., 2011] [Trindade et al., 2020]. This can in turn have an impact on the verification of the ERA* products. That is, since $ERA*_{ABC} N3$ contains more variance than the other two ERA* configurations ($ERA*_O N3$ and $ERA*_{ABCO} N3$), the verification with the relatively low variance HSCAT-B winds may result in larger VRMS values for the former than the latter ERA* configurations. Further verification with higher-resolution buoy U10S is therefore required to confirm that $ERA*_{ABCO} N3$ is indeed the optimal configuration. Note also, that the 3-sigma test applied to the scatterometer-ERA5 differences does not significantly alter the spectral slopes in Figs. 10 and 11.

It is clear from Figs. 10 and 11, that the size of the temporal window has a more pronounced effect on the spectral slope than the number of scatterometers used. Note also that whether we fix the number of scatterometers (Fig. 10) or the time window (Fig. 11), the spectra in the middle latitudes are more energetic at small wave numbers than those in the tropics, due to the presence of large-scale systems, still the same conclusions can be drawn in terms of spectral slopes.

World Ocean Circulation
Project Management Plan

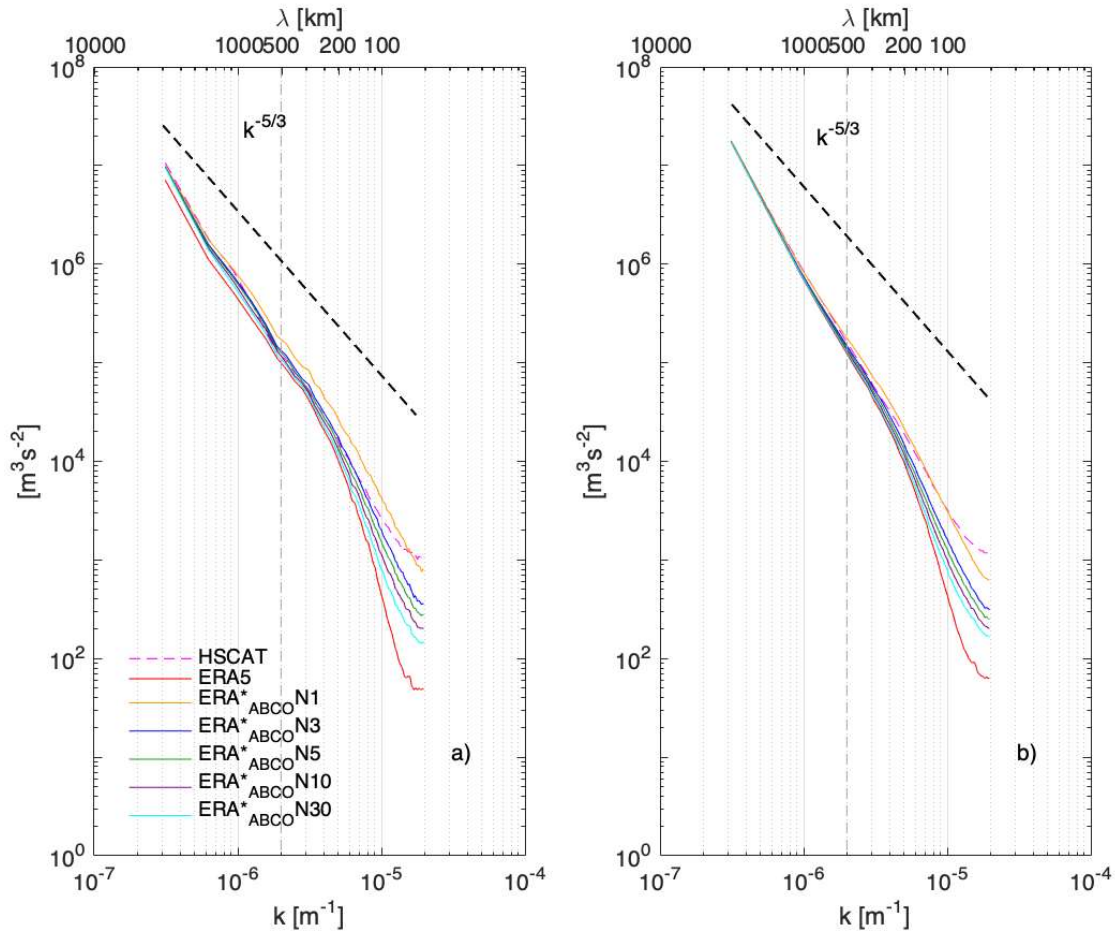Ref.: WOC-ESA-ODL-NR-
009_T1_ERAstar
Date: 30/06/2022
Issue: 2.0
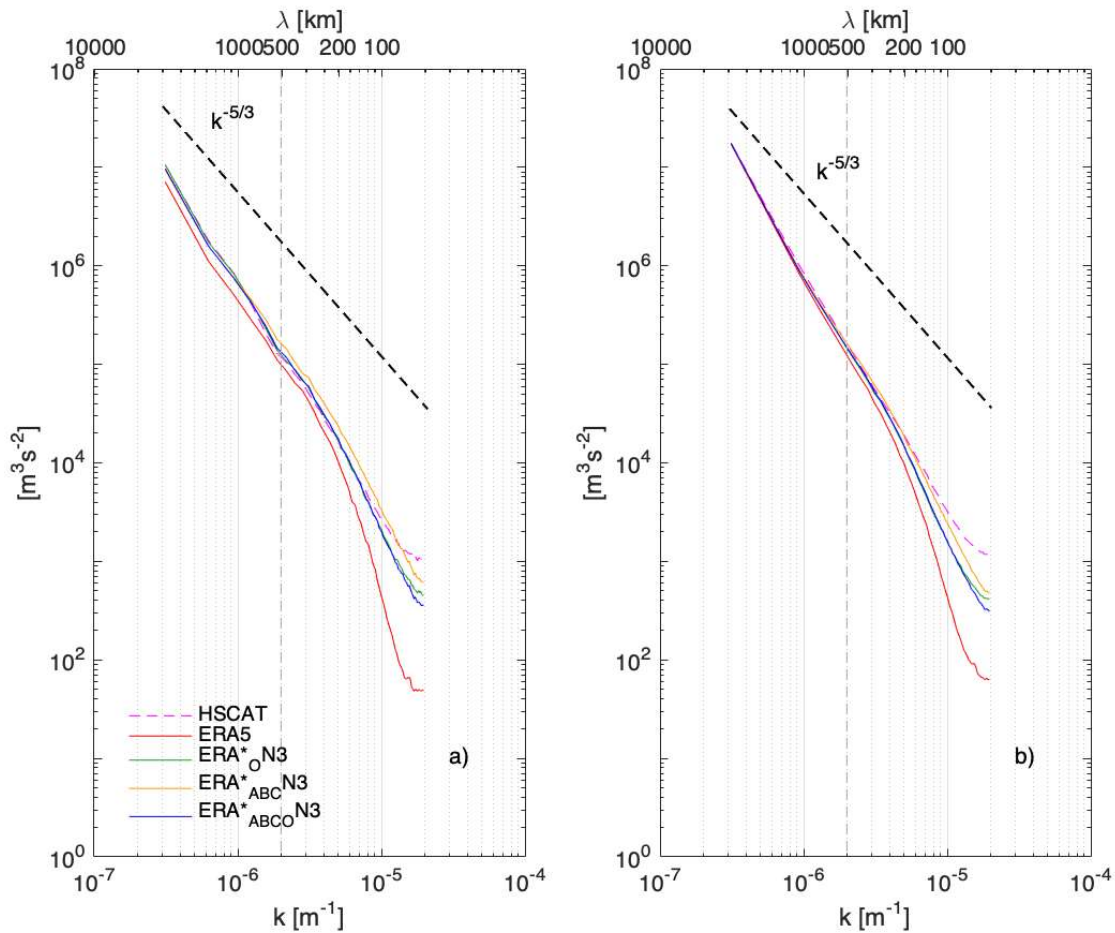
Figure 11. Power density spectra for the meridional U10S component of HSCAT-B (dashed pink) and collocated ERA5 (red) and ERA* (see colour legend) products, in the tropics (a) and the middle latitudes (b). The different ERA* configurations shown here use a 3-day SC temporal window (see notation in Table 1).

In summary, the ERA* method is regionally dependent, i.e., its effectiveness is mainly modulated by weather sampling and on the longer term by local bias persistence. Overall, we find that the ERA* configuration with the largest scatterometer sampling ($ERA*_{ABCO}$) provides the best performance approximately over a 3-day temporal window ($ERA*_{ABCO}N3$). Moreover, the 3-sigma filter applied to the scatterometer-ERA5 differences to remove transient weather effects results in further improvement of the ERA* quality. The $ERA*_{ABCO}N3$ relatively low VRMS scores and relatively shallow spectral slopes (in between those of HSCAT-B and ERA5) indicate that indeed smaller scale signal is introduced in the corrected ERA5 fields (i.e., ERA*).

World Ocean Circulation
Project Management Plan

Ref.: WOC-ESA-ODL-NR-
009_T1_ERAstar
Date: 30/06/2022
Issue: 2.0

2.5.4 Assessment of the varying scatterometer constellation

In the previous sections, it is concluded that an ERA* configuration based on a 3-day SC with maximized scatterometer sampling (i.e., ASCAT-A, -B, -C, and OSCAT2) provides the best performance. However, such optimal scatterometer sampling is only present for a few years within the 2010-2020 period. In this section, we assess the performance of the different scatterometer combinations present in the period of interest, using as validation reference both collocated buoy and independent scatterometer (HSCAT-B) U10S datasets for the year 2019.

Table 2 shows the list of available C- and Ku-band scatterometers for different periods within 2010-2020. Note that the optimized configuration (in terms of complementary sampling) of three ASCATs and one OSCAT is only available in the period 2019-2020. Other similar configurations, i.e., one or two ASCATs and one OSCAT, are available in 2010-2013 and 2017-2018. Finally, a 2-ASCATs only configuration is available in the 2014-2016 period. As such, the performance of the different scenarios needs to be tested before a nominal ERA* configuration is set for the entire period 2010-2020.

Table 2. Scatterometer constellation for different periods of time

Period	Scatterometer constellation
2010-2012	ASCAT-A, OSCAT
2013	ASCAT-A, ASCAT-B, OSCAT
2014-2016	ASCAT-A, ASCAT-B
2017-2018	ASCAT-A, ASCAT-B, OSCAT2
2019-2020	ASCAT-A, ASCAT-B, ASCAT-C, OSCAT2

Note that only scatterometers with global and (near) continuous coverage are listed in Table 2. Other Ku-band scatterometers with either regional (Rapidscat) or discontinued (HSCAT-A and HSCAT-B) coverage are used for validation purposes only. Also note that the following moored buoy arrays have been used for validation purposes: the National Data Buoy Center (NDBC) moored buoys off the coasts of USA, the Ocean Data Acquisition System (ODAS) buoys in the north-east Atlantic and British Isles inshore waters, the National Oceanic Atmospheric Administration (NOAA) Tropical Ocean Atmosphere (TAO) buoy arrays in the tropical Pacific, the Japan Agency for Marine-Earth Science and Technology (JAMSTEC) Triangle Trans-Ocean Buoy Network (TRITON) buoys in the western Pacific, the Prediction and Research Moored Array in the Atlantic (PIRATA), and the Research Moored Array for African–Asian–Australian Monsoon Analysis and Prediction (RAMA) at the tropical Indian Ocean. Fig. 12 shows the location of the moored buoy measurements used in here.
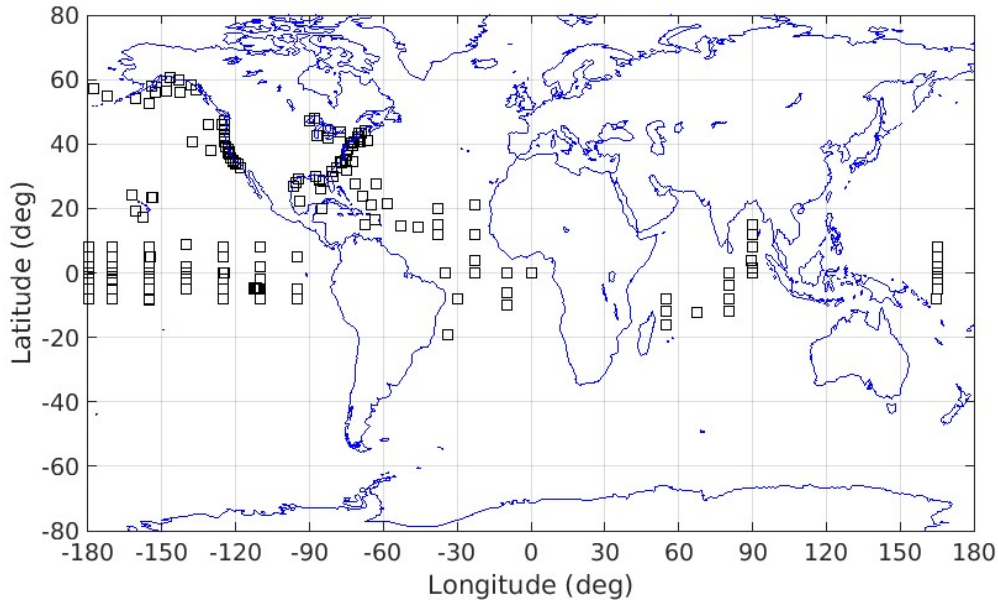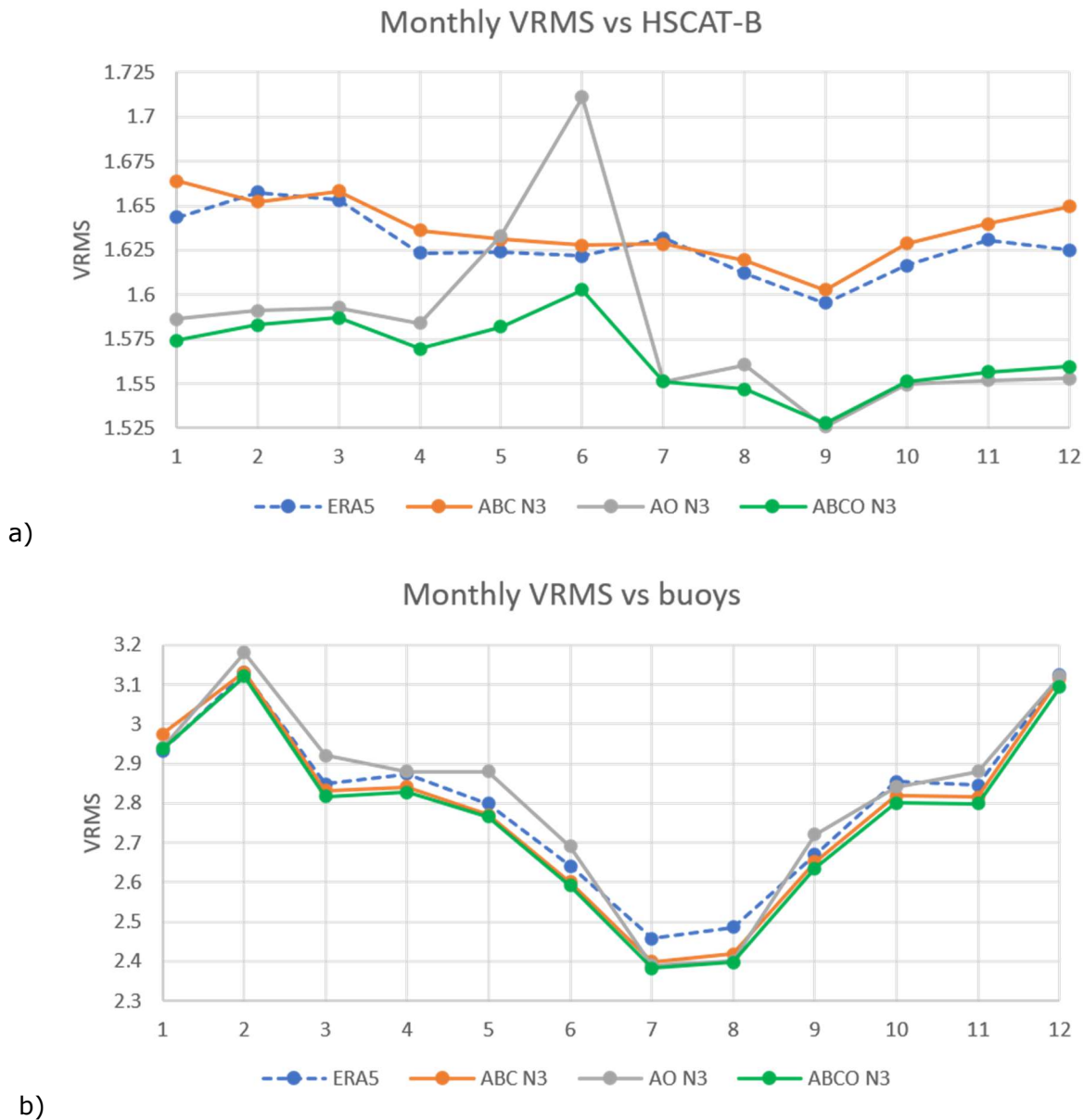
World Ocean Circulation
Project Management Plan

Ref.: WOC-ESA-ODL-NR-
009_T1_ERAstar
Date: 30/06/2022
Issue: 2.0

Figure 12. Map of the moored buoy locations used for validation purposes.

Fig. 13 shows the monthly ERA5 and ERA* verification against HSCAT-B (left) and buoy (right) U10S data. Different ERA* configurations (see legend) are tested, according to the different scatterometer constellations shown in Table 2 (note that $ERA *_{ABC} N3$ is shown instead of $ERA *_{AB} N3$, i.e., a more favorable configuration in terms of sampling). According to HSCAT-B verification (see Fig. 13a), it is clear that for a 3-day temporal window, only those combinations of ASCAT and OSCAT scatterometers ($ERA *_{AO} N3$ and $ERA *_{ABCO} N3$), which are rather complementary in terms of sampling, outperform the ERA5 product. Note also that for the months of May and June 2019, there is a degradation of the ERA* quality for those ERA* configurations that include OSCAT data. This is due to an OSCAT data interruption of about 30 days, which will be further analyzed in section 2.5.5. The ASCATs-only configuration ($ERA *_{ABC} N3$) generally shows slightly lower U10S quality than that of ERA5.

According to buoy verification (see Fig. 13b), $ERA *_{ABCO} N3$ generally outperforms ERA5. However, the ERA* quality improvement with respect to ERA5 is smaller than that observed in Fig 13a. Moreover, in contrast to the HSCAT-B verification results, $ERA *_{AO} N3$ ($ERA *_{ABC} N3$) generally shows a small quality degradation (improvement) with respect to ERA5. This needs further investigation. While buoy verification is local, i.e., over a few locations in the tropics and coastal areas (see Fig. 12), HSCAT-B verification is global. As such, local sampling patterns of the different ERA* configurations (e.g., the 12.5-km ASCATs have improved coastal sampling than the 25-km OSCATs) may play a more dominant role in the buoy than in the HSCAT-B verification. Note also that buoys measure earth fixed-relative winds. HSCAT-B observations, unlike buoys, are accurate relative to ocean surface currents that resolve the same oceanic variability scales that ERA* intends to capture. As such, independent scatterometers are used as the main validation reference in this document.

World Ocean Circulation
Project Management Plan

Ref.: WOC-ESA-ODL-NR-
009_T1_ERAstar
Date: 30/06/2022
Issue: 2.0

a)

b)

Figure 13. Monthly Vector root mean square (VRMS in ms^{-1}) difference between different ERA5/ERA* U10S products and HSCAT-B (a) and buoy (b) U10S, for a temporal window of 3 days and the following ERA* configurations: ASCAT-A/B/C (orange), ASCAT-A and OSCAT2 (grey), ASCAT-A/B/C and OSCAT2 (green). The ERA5 VRMS (blue dashed line) is also shown.

Fig. 14 shows the performance of ERA* for different ASCAT-only combinations using a 15-day and 30-day temporal window. It is clear that when 2 or more ASCATs are used, ERA* outperforms ERA5 (see the red curve below the dark blue dashed curve). For only one-ASCAT configuration, the 15-day time window leads to an ERA* quality similar to that of ERA5 (not shown), while the 30-day time window provides better quality U10S than ERA5 (see purple curve below the dark blue dashed curve).
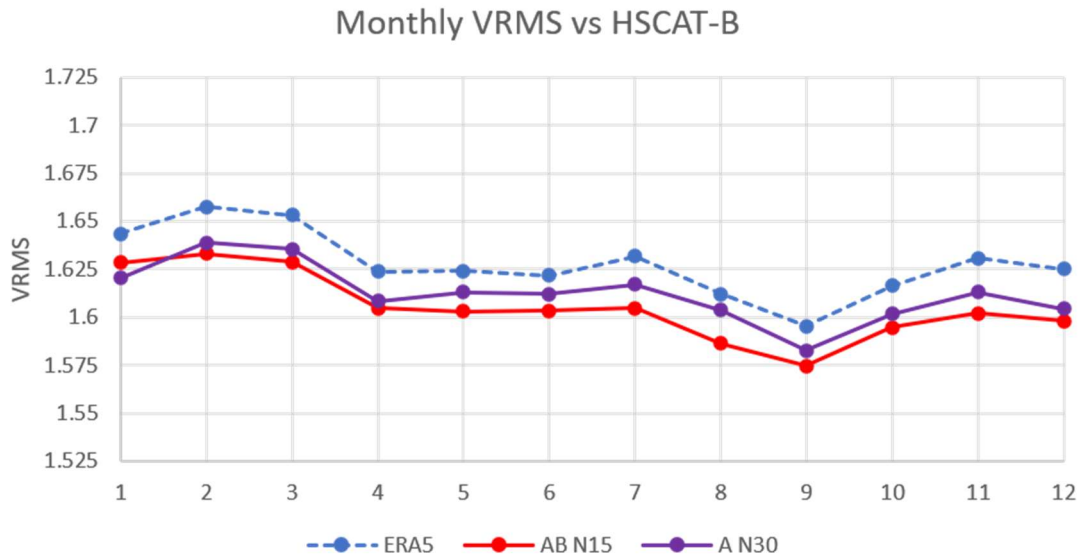
World Ocean Circulation
Project Management Plan

Ref.: WOC-ESA-ODL-NR-
009_T1_ERAstar
Date: 30/06/2022
Issue: 2.0

Figure 14. Monthly Vector root mean square (VRMS in ms^{-1}) difference between different ERA5/ERA* U10S products and HSCAT-B U10S, for two different ERA* configurations: ASCAT-A/B & 15-day temporal window (red), and ASCAT-A only & 30-day window (purple). The ERA5 VRMS is also shown (dark blue dashed line).

2.5.5 Data gap analysis

In this section, a more detailed analysis of the impact of the OSCAT2 data gap in May-June 2019 (see section 2.5.4) is carried out. In particular, the main data gap is from May 20th to June 19th, 2019 (see yellow-shaded period in Fig. 15).

Fig. 15 shows daily VRMS estimates of ERA5/ERA* versus HSCAT-B for the months of May and June 2019, for the ERA* configuration with ASCAT-A/-B/-C and OSCAT2 ($ERA*_{ABCO}$) and the following temporal windows: 3 (green), 15 (orange), and 30 (light blue) days. As expected, the 3-day temporal window provides the lowest VRMS scores, except for the OSCAT2 gap period. In this period, the 3-day window generally has a lower performance (higher VRMS) than the ERA5 product. That is, for OSCAT2 long data gaps (more than a day or so), the 3-day window does not provide sufficient sampling to outperform ERA5 U10S. As such, a longer temporal window of at least 15 days is needed. Note also that, when there are no data gaps, a 15-day time window leads to better ERA* performance than a 30-day time window.

Fig. 16 shows the same as Fig. 15 but for an ERA* configuration with ASCAT-A and OSCAT2 only ($ERA*_{AO}$). Again, the 3-day window is optimal for the data availability period. However, for the OSCAT2 data gap period, the ERA* quality is very much degraded. Although the 15-day configuration is of much higher quality than the 3-day configuration, it is clear that for an ASCAT-A only configuration ($ERA*_A$, resulting from the OSCAT2 gap), a 30-day time window is required for ERA* to outperform ERA5. In other words, $ERA*_A N30$ is the only ASCAT-A only configuration that leads to better U10S performance than that of ERA5.

World Ocean Circulation
Project Management Plan

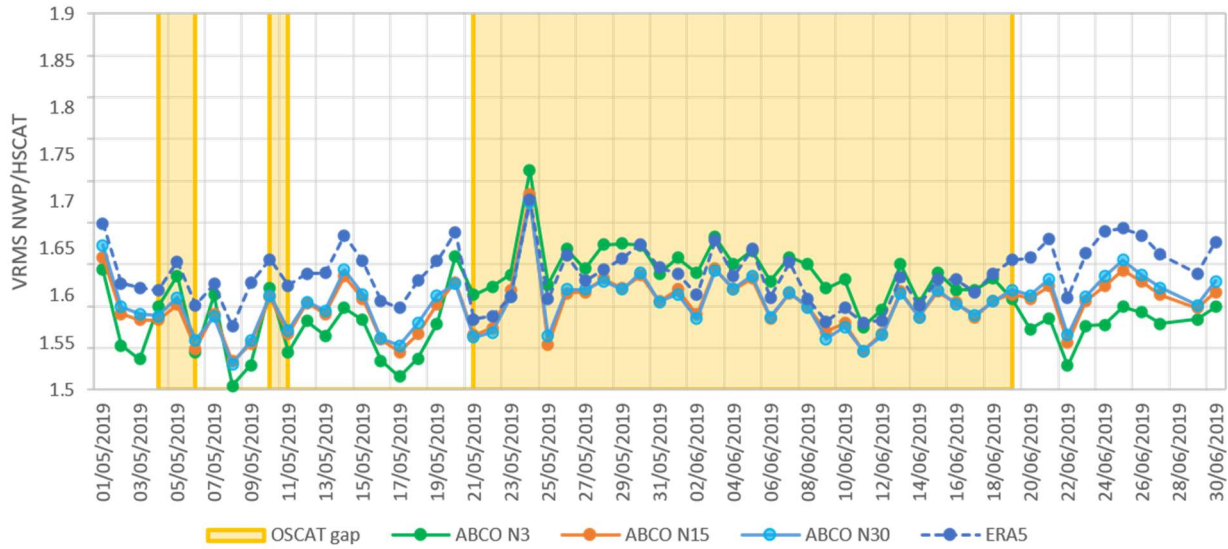Ref.: WOC-ESA-ODL-NR-
009_T1_ERAstar
Date: 30/06/2022
Issue: 2.0

Figure 15. Daily Vector root mean square (VRMS in ms^{-1}) difference between different ERA5/ERA* U10S products and HSCAT-B, for an ERA* configuration with ASCAT-A/B/C and OSCAT2 and the following temporal windows: 3 (green), 15 (orange), and 30 (light blue) days. The ERA5 VRMS (dark blue dashed line) is also shown. Note that the OSCAT2 data gap periods are shaded in yellow.
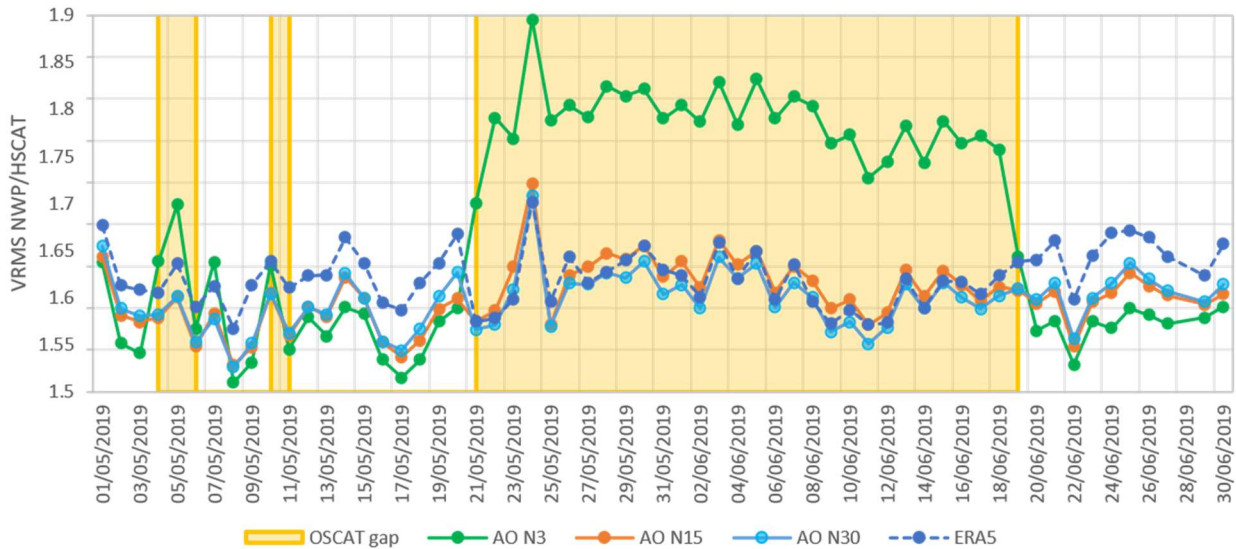

Figure 16. Same as Fig. 15 but for an ERA* configuration based on ASCAT-A and OSCAT2 only.

World Ocean Circulation
Project Management Plan

Ref.: WOC-ESA-ODL-NR-
009_T1_ERAstar
Date: 30/06/2022
Issue: 2.0

Fig. 17 shows a scatterplot of the daily VRMS scores of ERA* versus ERA5 over the year 2019, for the following ERA* configurations: ASCAT-A/-B/-C & OSCAT2 (left) and ASCAT-A & OSCAT2 (right) for two different temporal windows of 3 and 15 days. Note that the colored bullets lying above the diagonal represent the days in which ERA5 outperforms ERA*. These days mostly correspond to the mentioned OSCAT2 data gap period (between May and June 2019). Although it is clear that the 3-day window configuration shows the best performance most of the time (see green and blue bullets generally below the orange and red bullets, respectively), to minimize the amount of days in which the bullets lie above the diagonal (indicating an ERA* product outperforming ERA5 most of the time), a longer temporal window of 15 days needs to be used (see orange bullets almost always below the diagonal). Also, in line with the results in Fig. 16, it is clear that a 15-day window leads to ERA* poor-quality results for an ASCAT-A & OSCAT configuration when long OSCAT2 data gaps are present (see the excess of red bullets above the diagonal in the right panel of Fig. 17). A longer temporal window of 30 days is therefore needed in these cases.
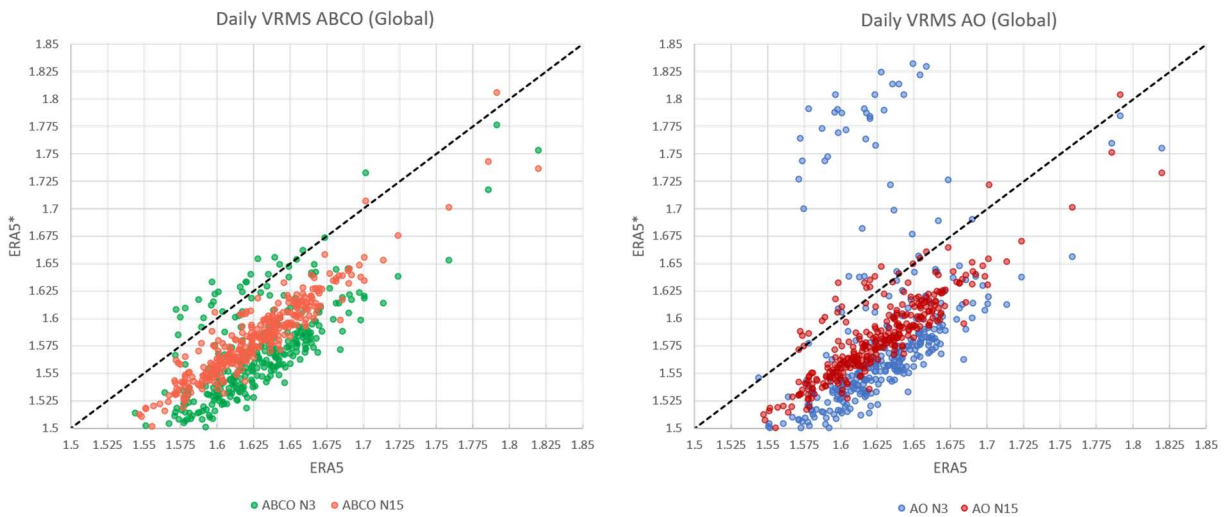

Figure 17. Scatterplot of the daily VRMS scores (against HSCAT-B) of ERA* versus ERA5 over the year 2019, for the following ERA* configurations: ASCAT-A/-B/-C & OSCAT2 (left) and ASCAT-A & OSCAT2 (right) for two different temporal windows of 3 (green, left; blue, right) and 15 (orange, left; red, right) days.

Fig. 18 shows the number of accumulated data gaps (in days) per year, for the different scatterometers (see legend) in the period 2010-2020. Below the x-axis label, the different scatterometer sampling combinations is specified for every year (see also Table 2). It is clear that the largest data gaps correspond to the OSCAT and OSCAT2 scatterometers, while only a few data gaps of ASCAT-A and ASCAT-C are present during the entire 2010-2020 period. In particular, more than 30 days of accumulated data gaps are present in OSCAT or OSCAT2 for the years 2010, 2011, 2017, and 2019. Also, in the period 2014-2016, only two ASCATs are available.
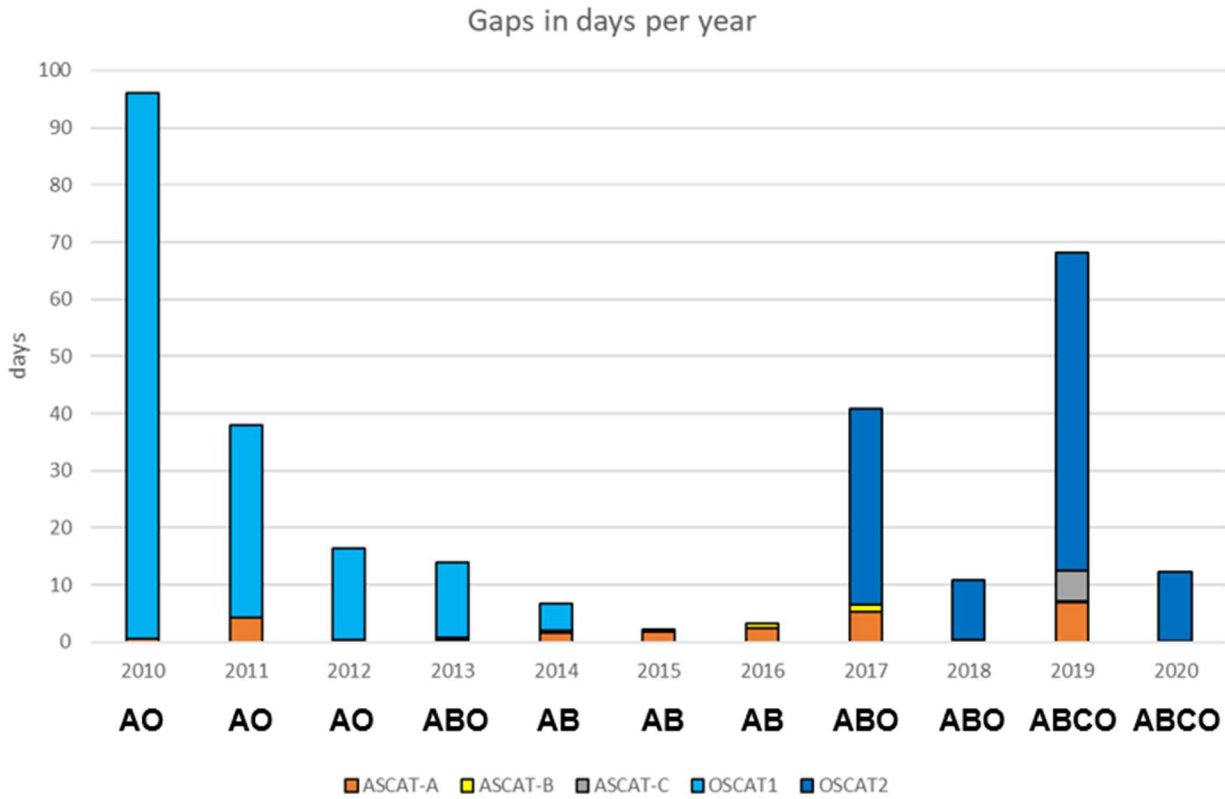
Figure 18. Number of accumulated data gaps (in days) per year, for the different scatterometers (see legend) in the period 2010-2020. Below the x-axis label, the different scatterometer sampling combination is specified for every year: ASCAT-A & OSCAT (AO), ASCAT-A/-B & OSCAT (ABO), ASCAT-A/-B (AB), ASCAT-A/-B & OSCAT2 (ABO), ASCAT-A/-B/-C & OSCAT2 (ABCO).

Given the performance of the different ERA* configurations shown in sections 2.5.4 and 2.5.5, and the important OSCAT and OSCAT2 data gaps shown in Fig. 18, a baseline ERA* configuration with a temporal window of 15 days is proposed. In 2010 though, since the OSCAT data is missing for more than 3 months, a 30-day temporal window is proposed instead. A summary of the ERA* baseline configurations is provided in Table 3.

Table 3. ERA* baseline configurations for the period 2010-2020.

ERA* configuration	Period
$ERA*_{AO} N30$	2010
$ERA*_{AO} N15$	2011-2012
$ERA*_{ABO} N15$	2013
$ERA*_{AB} N15$	2014-2016
$ERA*_{ABO} N15$	2017-2018
$ERA*_{ABCO} N15$	2019-2020

World Ocean Circulation
Project Management Plan

Ref.: WOC-ESA-ODL-NR-
009_T1_ERAstar
Date: 30/06/2022
Issue: 2.0

An enhanced-quality ERA* configuration using a 3-day temporal window is also proposed for the years 2013, 2018, and 2020, periods in which the OSCAT or OSCAT2 accumulated data gaps are relatively small. A summary of the ERA* enhanced-quality configurations is provided in Table 4.

Table 4. ERA* enhanced configurations.

ERA* configuration	Period
$ERA *_{ABO} N3$	2013 & 2018
$ERA *_{ABCO} N3$	2020

2.5.6 Verification of the selected ERA* configurations

Fig. 19 shows the mean error variance reduction (in %, w.r.t. that of ERA5) of the selected 15-day ERA* configurations against independent scatterometer U10S data. Note that in 2010, no independent scatterometer is available for verification purposes. As such, no verification of the $ERA *_{AO} N30$ configuration is carried out in 2010. However, it is clear from the verification of 2019 (see previous sections), that the $ERA *_{AO} N30$ configuration outperforms ERA5 (see Fig. 16), even when long OSCAT2 data gaps exist, thus effectively becoming $ERA *_A N30$ (see Fig. 14).

Overall, the nominal ERA* 15-day product outperforms ERA5 with an error variance reduction of about 3-9%, depending on the ocean region and the scatterometer combination. Those ERA* configurations using a combination of C- (ASCATs) and Ku- (OSCATs) band scatterometers lead to the best performances. Note also that the largest sampling configuration ($ERA *_{ABCO} N15$) show slightly lower error variance reductions than the other configurations ($ERA *_{AO} N15$ or $ERA *_{ABO} N15$). This may be due to the fact that different periods of time and independent scatterometers are used in the verification of the different configurations. [Note also that the OSCAT & OSCAT2 data gaps shown in Fig. 18 also impact the ERA* N15 configurations, although the impact on the yearly or 2-yearly scores of Fig. 19 is actually small (not shown)]. However, it may also indicate that there is a trade-off between sampling and temporal window size, i.e., for sufficient sampling, a smaller temporal window is preferred since some ERA5 local biases may not persist over 2 weeks, but over shorter temporal scales. However, because of the mentioned long OSCAT and OSCAT2 data gaps, a rather conservative approach (to ensure sufficient sampling over the gap periods) is followed for the baseline product.

Fig. 20 shows the mean error variance reduction (in %, w.r.t. that of ERA5) of the enhanced 3-day ERA* configurations against independent scatterometer U10S data for the selected periods, i.e., 2013, 2018, and 2020. Overall, the nominal ERA* 3-day product outperforms ERA5 with an error variance reduction of about 6-11%, depending on the ocean region and the scatterometer combination. As expected for short temporal windows, the ERA* configuration with the largest sampling ($ERA *_{ABCO} N3$) leads to the highest quality U10S. While in the tropics and the high latitudes, $ERA *_{ABCO} N3$ outperforms ERA5 with an error variance reduction larger than 10%, in the middle latitudes the error reduction is smaller, around 6%. Globally, the $ERA *_{ABCO} N3$ error variance is about 9% lower than that of ERA5.
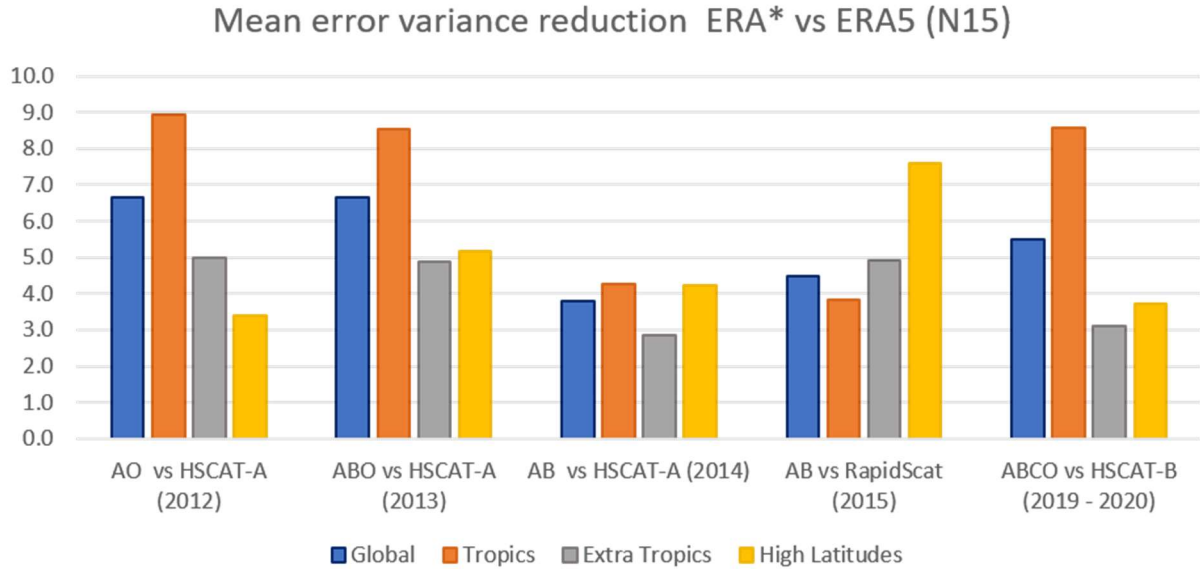
Figure 19. Mean error variance reduction (in percentage, with respect to that of ERA5) of the selected ERA* 15-day configurations against independent scatterometers for global, tropical, extra-tropical, and high-latitude regions (see legend). In particular, $ERA*_{AO}N15$, $ERA*_{ABO}N15$, and $ERA*_{AB}N15$ are verified against HSCAT-A, respectively in 2012 (only second half of the year), 2013, and 2014; $ERA*_{AB}N15$ is verified against Rapidscat in 2015; and $ERA*_{ABCO}N15$ is verified against HSCAT-B in 2019-2020.
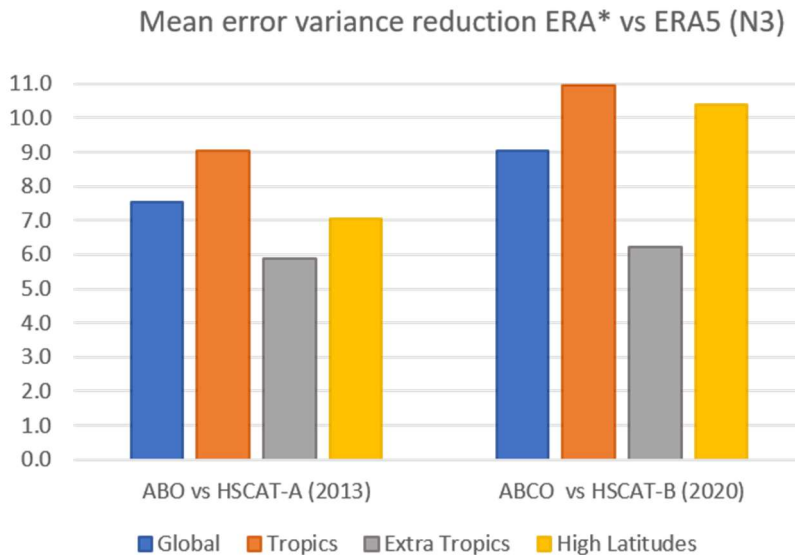

Figure 20. Mean error variance reduction (in percentage, with respect to that of ERA5) of the ERA* 3-day configurations against independent scatterometers for global, tropical, extra-tropical, and high-latitude regions (see legend). In particular, ABO is verified against HSCAT-A in 2013; and ABCO is verified against HSCAT-B in 2020.

Future work will focus on mitigating the across-track biases in Ku-band scatterometer-derived U10S fields, further reducing the transient weather effects and characterizing low sampling effects in the computation of the SC (e.g., in coastal areas).

Moreover, we now understand that the NWP wind vector biases are linked to atmospheric stability effects, moist convection, ocean currents, etc. As such, we plan to employ deep learning methods built upon NWP forecast fields of ocean vector winds and associated ocean surface and atmosphere parameters to predict SC, leading to corrected and hence better-quality NWP surface wind and stress fields for both atmospheric and oceanic applications.

3 References

[Belmonte-Rivas and Stoffelen, 2019] M. Belmonte-Rivas and A. Stoffelen, "Characterizing ERA-Interim and ERA5 surface wind biases using ASCAT," Ocean Sci., vol. 15, no. 3, pp. 831–852, 2019.

[Brown et al., 2005] A. R. Brown, A. C. M. Beljaars, H. Hersbach, A. Hollingsworth, M. Miller, and D. Vasiljevic, "Wind turning across the marine atmospheric boundary layer," Quart. J. Roy. Meteorol. Soc., vol. 131, no. 607, pp. 1233–1250, 2005.

[Chelton and Xie, 2010] D. B. Chelton and S.-P. Xie, "Coupled ocean-atmosphere interaction at oceanic mesoscales," Oceanography, vol. 23, no. 4, pp. 52–69, Dec. 2010.

[Chelton et al., 2006] D. B. Chelton, M. H. Freilich, J. M. Sienkiewicz, and J. M. Von Ahn, "On the use of QuikSCAT scatterometer measurements of surface winds for marine weather prediction," Monthly Weather Rev., vol. 134, no. 8, pp. 2055–2071, Aug. 2006.

[Chelton and Freilich, 2005] D. B. Chelton and M. H. Freilich, "Scatterometer-based assessment of 10-m wind analyses from the operational ECMWF and NCEP numerical weather prediction models," Amer. Meteorol. Soc., vol. 133, no. 2, pp. 409–429, Feb. 2005.

[Chelton et al., 2004] D. B. Chelton, M. G. Schlax, M. H. Freilich, and R. F. Milliff, "Satellite measurements reveal persistent small-scale features in ocean winds," Science, vol. 303, no. 5660, pp. 978–983, 2004.

[De Kloe et al., 2017] J. De Kloe, A. Stoffelen, and A. Verhoef, "Improved use of scatterometer measurements by using stress-equivalent reference winds," IEEE J. Sel. Topics Appl. Earth Observat. Remote Sens., vol. 10, no. 5, pp. 2340–2347, May 2017.

[Driesenaar et al., 2020] Driesenaar et al., "CMEMS Quality Information Document for the Global Ocean L3 Wind products," CMEMS-WIND-QUID-012-002-003-005, Issue 1.14, KNMI, De Bilt, The Netherlands, available from https://marine.copernicus.eu/, 2020.

[Edson et al., 2013] Edson, J. B., Jampana, V., Weller, R. A., Bigorre, S. P., Plueddemann, A. J., Fairall, C. W., Miller, S. D., Mahrt, L., Vickers, D., and Hersbach, H., "On the Exchange of Momentum over the Open Ocean," Journal of Physical Oceanography, 43(8), 1589–1610, 2013.

[Hersbach et al., 2020] H. Hersbach et al., "The ERA5 global reanalysis," Quart. J. R. Met. Soc., 146 (730), pp. 1999-2049, https://doi.org/10.1002/qj.3803, 2020.

[Hersbach, 2010] H. Hersbach, "Comparison of C-band scatterometer CMOD5.N equivalent neutral winds with ECMWF," J. Atmos. Ocean. Technol., vol. 27, no. 4, pp. 721–736, Apr. 2010.

[Hoareau et al., 2018] Hoareau, N., Turiel, A., Portabella, M., Ballabrera-Poy, J., and Vogelzang, J., "Singularity Power Spectra: A method to assess geophysical consistency of gridded products - Application to sea-surface salinity remote sensing maps," IEEE Trans. Geosci. Rem. Sens., 56 (9), pp. 5525-5536, https://doi.org/10.1109/TGRS.2018.2819240, 2018.

[Kelly et al., 2001] K. A. Kelly, S. Dickinson, M. J. McPhaden, and G. C. Johnson, "Ocean currents evident in satellite wind data," Geophys. Res. Lett., vol. 28, no. 12, pp. 2469–2472, Jun. 2001.

[King et al., 2017] G. P. King, M. Portabella, W. Lin, and A. Stoffelen, "Correlating extremes in wind and stress divergence with extremes in rain over the Tropical Atlantic," EUMETSAT OSI SAF, Hamburg, Germany, Tech. Rep SAF/OSI/CDOP3/KNMI/SCI/RP/312, version 1.0, 2017.

[Lin and Portabella, 2017] Lin, W., and Portabella, M., "Towards an improved wind quality control for RapidScat," IEEE Trans. Geosci. Rem. Sens., 55 (7), pp. 3922-3930, https://doi.org/10.1109/TGRS.2017.2683720, 2017.

[Lin et al., 2015a] W. Lin, M. Portabella, A. Stoffelen, A. Verhoef, and A. Turiel, "ASCAT

Wind quality control near rain," IEEE Trans. Geosci. Remote Sens., vol. 53, no. 8, pp. 4165–4177, Aug. 2015.

[Lin et al., 2015b] Lin, W., Portabella, M., Stoffelen, A., Vogelzang, J., and Verhoef, A., "ASCAT wind quality under high subcell wind variability conditions," J. Geophys. Res. Oceans, 120 (8), pp. 5804–5819, https://doi.org/10.1002/2015JC010861, 2015.

[Nastrum and Gage, 1985] Nastrum, G.D, and Gage, K.S., "A Climatology of Atmospheric Wavenumber Spectra of Wind and Temperature Observed by Commercial Aircraft," Journal of the Atmospheric Sciences 42(9), 950-960, 1985.

[Portabella et al., 2021] Portabella, M., Trindade, A., Grieco, G., and Makarova, E., "World Ocean Circulation Product User Manual for ERAstar (Theme 1)," WOC-ESA-ODL-NR-010_T1_ERAstar_V1.0, 2021.

[Portabella and Stoffelen, 2009] M. Portabella and A. Stoffelen, "On scatterometer ocean stress," J. Atmos. Ocean. Technol., vol. 26, no. 2, pp. 368–382, Feb. 2009.

[Portabella and Stoffelen, 2004] Portabella, M., and Stoffelen, A., "A probabilistic approach for SeaWinds data assimilation," Quart. J. R. Met. Soc., 130 (596), pp. 127-152, https://doi.org/10.1256/qj.02.205, 2004.

[Reynolds and Chelton, 2010] R. W. Reynolds and D. B. Chelton, "Comparisons of daily sea surface temperature analyses for 2007–08," J. Climate, vol. 23, no. 13, pp. 3545–3562, 2010.

[Sandu et al., 2013] I. Sandu, A. Beljaars, P. Bechtold, T. Mauritsen, and G. Balsamo, "Why is it so difficult to represent stably stratified conditions in numerical weather prediction (NWP) models?" J. Adv. Model. Earth Syst., vol. 5, no. 2, pp. 117–133, 2013.

[Stoffelen and Vogelzang, 2018] A. Stoffelen and J. Vogelzang, "Wind bias correction guide," EUMETSAT, Darmstadt, Germany, Tech. Rep. NWPSAF-KN-UD-007, v1.3, Sep. 2018.

[Tang et al., 2014] W. Tang, W. T. Liu, B. Stiles, and A. Fore, "Detection of diurnal cycle of ocean surface wind from space-based observations," Int. J. Remote Sens., vol. 35, no. 14, pp. 5328–5341, 2014.

[Trindade et al., 2020] Trindade, A., Portabella, M., Stoffelen, A., Lin, W., and Verhoef, A., "ERAstar: a high resolution ocean forcing product", IEEE Trans. Geosci. Rem. Sens., 58 (2), pp. 1337-1347, https://doi.org/10.1109/TGRS.2019.2946019, 2020.

[Verhoef et al., 2020] Verhoef, A., Vogelzang, J., Verspeek, J., and Stoffelen, A., "AWDP User Manual and Reference Guide," EUMETSAT OSI SAF, NWPSAF-KN-UD-005, v3.3, available from https://nwp-saf.eumetsat.int/, 2020.

[Verhoef et al., 2018] Verhoef, A., Vogelzang, J., Verspeek, J., and Stoffelen, A., "PenWP User Manual and Reference Guide," EUMETSAT OSI SAF, NWPSAF-KN-UD-009, v2.2, available from https://nwp-saf.eumetsat.int/, 2018.

[Vogelzang et al., 2015] J. Vogelzang, G. P. King, and A. Stoffelen, "Spatial variances of wind fields and their relation to second-order structure functions and spectra," J. Geophys. Res., Oceans, vol. 120, no. 2, pp. 1048–1064, 2015.

[Vogelzang et al., 2013] J. Vogelzang, "How to calculate wind spectra," EUMETSAT, Darmstadt, Germany, Tech. Rep. NWPSAF-KN-TR-008, v1.1, Apr. 2013.

[Vogelzang et al., 2011] J. Vogelzang, A. Stoffelen, A. Verhoef, and J. Figa-Saldaña, "On the quality of high-resolution scatterometer winds," J. Geophys. Res., Oceans, vol. 116, no. C10, pp. 1–14, Oct. 2011.

[Wang et al., 2019] Wang, Z., Stoffelen, A., Zhang, B., He, Y., Lin, W., Li, X., "Inconsistencies in scatterometer wind products based on ASCAT and OSCAT2 collocations," Remote Sensing of Environment, 225, 207-216, doi:10.1016/j.rse.2019.03.005, 2019.